ETH
Eidgenössische Technische Hochschule Zürich
Swiss Federal Institute of Technology Zurich

Empa
Materials Science and Technology

Fatigue Analysis of Selective Laser Melted Ti6Al4V Structures

Max Thalmann

Bachelor Thesis

February 14, 2020

Advisors: Prof. Dr E. Mazza, Dr E. Hosseini, Dr K. Schillai

306 - Experimental Continuum Mechanics, Empa, ETH Zürich

Acknowledgements

Firstly, I would like to thank the *Experimental Continuum Mechanics Lab* and Prof. Dr Edoardo Mazza for the opportunity of doing my bachelor thesis there.

Special thanks belong to my advisors, Dr Ehsan Hosseini and Dr Kilian Schillai who continuously supported and backed my project with great interest and enthusiasm.

Finally, I am highly grateful and appreciate the willingness of all colleagues in the lab to help out and answer my project-related questions. In this regard, I would like to highlight doctoral candidate Pooriya Gh Ghanbari for the help with all questions concerning simulating on the *Euler* cluster and Dr Kilian Schillai for the help with the microscope.

Contents

List of Abbreviations

AM	Additive Manufacturing
BC	Boundary Condition
CAD	Computer-Aided Design
FE	Finite Element
FEA	Finite Element Analysis
HCF	High Cycle Fatigue
HIP	Hot Isostatic Pressing
SLM	Selective Laser Melting
μ-CT	Micro Computer Tomography

List of Symbols

$\boldsymbol{\sigma}$	Stress Tensor in 3D
$\sigma_1, \sigma_2, \sigma_3$	Principal Stresses in 3D
σ_a	Stress Amplitude
σ_m	Average Stress
σ_{max}	Maximal Stress
σ_{min}	Minimal Stress
σ_{nom}	Nominal Stress
σ_f	Fatigue Limit Stress
σ_{top}	Load for Struts in Simulations
$\sigma_{v,M}$	Mises Stress
a_0	Initial Crack Length
a_f	Final Crack Length
A_{nom}	Nominal Cross-Section of Struts
ΔK	Stress Intensity Range
K	Stress Intensity Factor
K_t	Stress Concentration Factor
N_f	Number of Cycles until Failure
R	Stress Ratio
R_{Area}	Area Ratio for Struts
ΔS	Testing Stress Difference

Chapter 1

Introduction

1.1 Motivation

In recent years, the impact of additive manufacturing (AM) grew largely.[10] It is a new production method with many interesting new possibilities compared to conventional manufacturing. Its unique characteristics make it especially interesting for specific applications in the fields of aerospace/space or biomedical engineering. It brings advantages like an incomparably large design freedom and the possibility to manufacture extremely lightweight parts, which qualify this technology to fabricate a wide range of functionally integrated parts.[10] Process details are discussed in section 1.2.

In particular, it is possible to create cellular structures to a predefined stiffness and porosity. With this flexibility, AM is highly interesting for the fabrication of medical implants. With the high porosity, the structures enable possible bone ingrowth and the surface coating of certain well-suited areas with pharmaceutical active agents such as pain killers or anti-inflammatory drugs. The adjustability of the structure's stiffness provides a solution to possibly minimize the risk of bone degeneration around the implant due to stress shielding effects.

The production process of AM is comparable to a welding process. Therefore, the mechanical properties of additively manufactured material differ significantly compared to conventionally manufactured materials. Numerous ongoing researches try to describe the material properties of AM materials. Anisotropic material behaviour and often inferior mechanical properties are reported.

Most studies research the behaviour under static loads and only a few investigate the fatigue behaviour properties. Tests have shown that even if a cellular structure behaves excellently under static loading, it is often prone to fail under comparably small dynamic loads.[15] & [6]

1.2 Additive Manufacturing

In contrast to conventional manufacturing - which starts out from a block of solid material and removes material (milling, lathing, drilling, etc.) - the raw material for AM is either a fine powder of the material or a filament, which is deployed layer by layer creating the designed structure.[1] Therefore, the material synthesis and manufacturing of the final product happen simultaneously. This is a big advantage of AM which brings a large design freedom and the possibilities to create geometrically highly complex configurations.[1] E.g. it is possible to create integrated hollow spirals into the wall of a tube or minimalistic foam like lattice structures.

There are different types of AM processes. The relevant one for this thesis is *Selective Laser Melting* (SLM). In this process, the part is built by the successively melting of new layers of powder. The melting is done by one or several laser beams. As for many 3D printing processes, the part is generated on a heated build platform, which is lowered by the pre-set layer thickness for each layer. To distribute the powder homogeneously over the build platform for each layer, it is distributed by a roller. All the leftover unmelted powder remains on the build platform until the end of the manufacturing process and serves as supporting material. Once the manufacturing process is finished, the powder is removed and the part can be post-processed with various heat treatments or surface refinements. A schematic visualization of an SLM printing machine can be found on the right side in Figure 1.1.

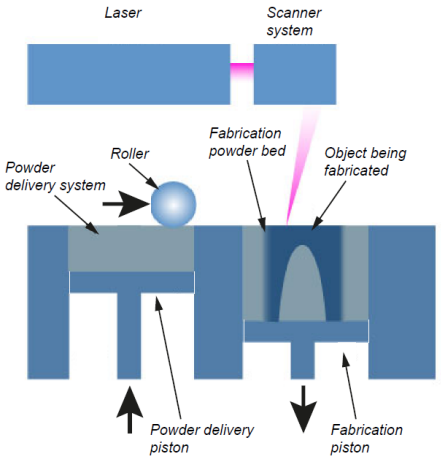

Figure 1.1: Schematic SLM process overview with the relevant elements.[3]

Due to its nature of melting layer by layer, the laser melts the top layer and simultaneously remelts and reheats previous layers. This influences the metallic grain growth significantly and leads to a typical *martensitic* grain structure. In section 2.3 there are two microscopic pictures of the grain structure of additively manufactured Ti-6Al-4V in Figure 2.7. Furthermore, compared to conventional manufacturing methods, the AM generated surface of a piece is best comparable to metal casting with a characteristical rough surface. SLM-printable materials include steels, ceramics, aluminium, titanium and many other metal alloys.

1.3 Fatigue Analysis

Fatigue analysis incorporates methods to predict and explain the behaviour of materials and structures under cyclic loading. According to J. Schijves [17], the fatigue life of a specimen is governed by two main phases, first, the *Initiation Period*, which is followed by the *Crack Growth Period* that ultimately leads to the final failure of the piece.

The difference between these phases, and the knowledge whether the problem at hand is initiation or propagation dominated, are the essentials for a good prediction of the performance. This is crucial since for each phase there are distinct properties and conditions that affect fatigue life or fatigue crack growth. With this distinction, the suitable relations can be applied.

For the initiation dominated cases, the common practice is to use the *Stress Concentration Factor* K_t, while for the propagation dominated ones, fracture mechanics and the *Stress Intensity Factor* K have to be considered for calculations.

1.3.1 Stress Concentration Factors

In the case of a crack initiation problem, the main focus lies upon the calculation of the *Stress Concentration Factors* K_t. The stress distribution is primarily based on the theory of elasticity.[17] If the local stresses exceed the yield limit, plastic deformation occurs and the more complex theory of plasticity needs to be consulted.

However, for *High Cycle Fatigue* (HCF) the fatigue phenomena usually occur at such small stresses where no plasticity occurs and the stresses are concentrated very locally around defects. Therefore, the *geometrical shape* of a specimen and its *notches* are the defining properties. At the *notches root*, the theoretical stress maxima σ_{max} are located. These maxima are always compared to a *nominal stress* σ_{nom}, which is often the value of the stress for an unnotched sample or the stress over the cross-section at the root of the notch. The ratio of $\sigma_{max}/\sigma_{nom}$ is then defined as the *Stress Concentration Factor* K_t for the particular notch. For a multitude of notches, the examined K_t-factors can be obtained from lookup tables or charts.[14] In general, the value of K_t rises the sharper a notch (the smaller the inner radius) is or the deeper a notch intrudes a structure.

The following two Figures 1.2 and 1.3 show two examples of geometries with well known notches out of the everyday use of engineers, the shoulder fillets for a flat or a round bar. The mentioned tendencies are well visible. For the theoretical 90°-*edge* the value for K_t rises to infinity. Further explanations on the topic of *Stress Concentration Factors* and their determination are discussed in section 2.2.

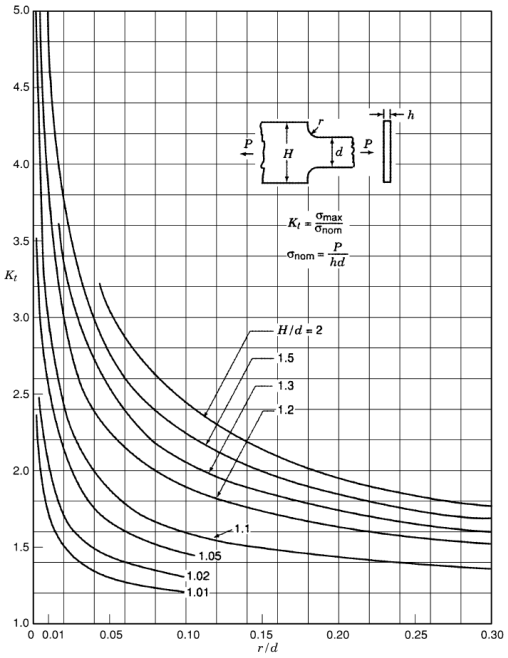

Figure 1.2: "Stress concentration factors K_t for a stepped flat tension bar with shoulder fillets (based on data of Frocht 1935; Appl and Koerner 1969; Wilson and White 1973)."[14]

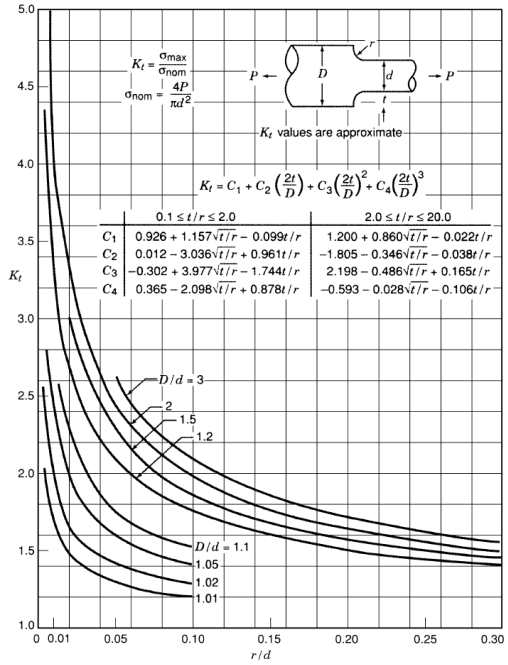

Figure 1.3: "Stress concentration factors K_t for a stepped tension bar with circular cross-section and shoulder fillet."[14]

1.3.2 S/N-Plots

For a first approach to determine the fatigue performance of a material or a structure one usually considers their *S/N - Curves*. Figure 1.4 shows such a diagram for Ti-6Al-4V made with different production methods. Since the experimental data has a significant scatter, the fatigue tests are repeatedly carried out under the same conditions. Finally, a line is fitted through the points such that the line represents a 90%-chance of survival. Figure 1.5 provides a schematic plot that describes the different lines one can read out of an *S/N - Plot*.

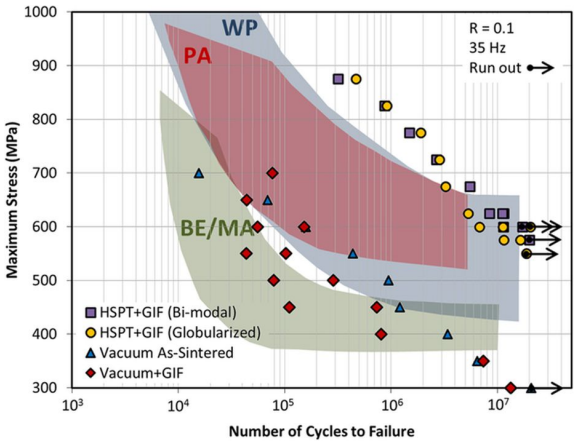

Figure 1.4: "Fatigue performance (S-N) curves for Ti-6Al-4V produced [...] via HSPT and gaseous isostatic forging (GIF) with subsequent heat treatment to produce bi-modal and globularized microstructures, as well as conventional vacuum sintering with and without GIF."[11]

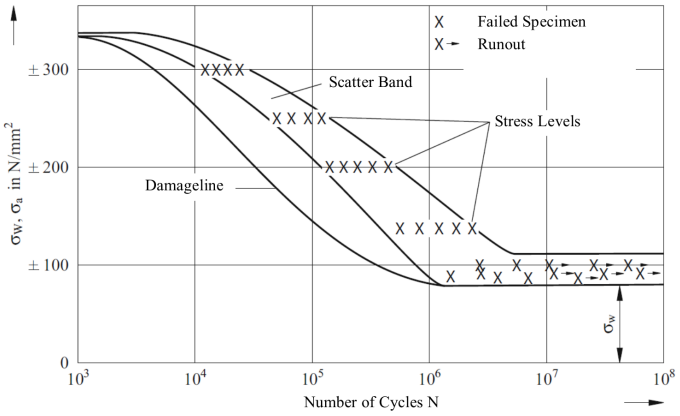

Figure 1.5: Schematic S/N - plot. Translated to English from [16].

1.3.3 Cracks

The following section about cracks is mainly based on the explanations from J. Schijves Book - *Fatigue of Structures and Materials*.[17]

The fatigue life of a specimen is defined by the number of repeated load cycles it can withstand before it rips apart. Thus the final failure is a breakage in the geometry. As mentioned before at the beginning of section 1.3 these types of ruptures are initiated by cracks. Figure 1.6 displays the different phases of the fatigue life and for each main period the dominating factor.

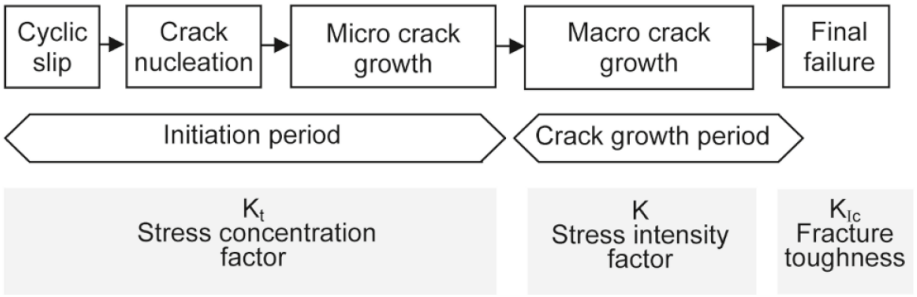

Figure 1.6: "Different phases of the fatigue life and relevant factors."[17]

There are two main possibilities of crack types: the ones where the fatigue life ends within only a few additional cycles after crack initiation with a close to inexistent propagation period and those for which the propagation period is dominating the better part of the lifespan. The former are labelled as *Crack Initiation Problems* and the latter as *Crack Propagation Problems*.

Crack Initiation

The initiation and the growth of cracks are a consequence of the phenomenon called *cyclic slip*. This describes the plastic deformation of a specimen along so-called *slip planes*. There is plastic deformation even though fatigue occurs at stress amplitudes significantly below the yield limit of a material.

Looking through the material on a microscale, the shear stresses are never homogeneously distributed and can locally reach large enough values to produce plastic deformation. The favourable locations to slip are mainly on the surface.[17] Figure 1.7 on the next page shows the basic mechanisms of cyclic slip. Once initiated, for each consecutive cycle of loading, the stress in the slip plane will increase. Cyclic slip leads to microcracks.

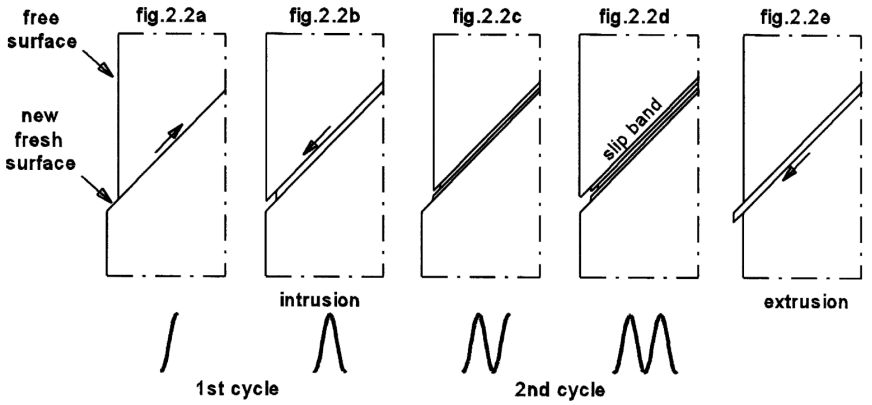

Figure 1.7: Mechanisms of Cyclic Slip [17]

Another reason for the slip to start on a geometry's surface are the introduced *stress concentrations* due to notches as in section 1.3.1 described. They lead to maximal stresses on the surface and in the notch's root. Therefore, the conditions there are favourable to slip initiation. This leads to the following two conclusions:

"In the crack initiation period, fatigue is a material surface phenomenon."[17]

and

"The initiation period is supposed to be completed when microcrack growth is no longer depending on the material surface conditions."[17]

After the initiation phase, the crack grows in size. Thus this is called the crack growth period, where the microcrack changes into a macro scale phenomenon.

Crack Growth

For the first phase of growth, the crack is still in one single grain of the material's microstructure. It contributes to an increased heterogeneity in the stress distribution. This distribution has its concentration peak at the tip of the crack. As soon as the crack grows into adjacent grains the slip changes from single plane to multiplane slip. In general, it will now expand normal to the loading direction. Due to the cyclic mechanisms of slipping the progression over grain boundaries causes a significant reduction in growth speed.[17] Different grains are due to different orientation and anisotropy

differently affected by stresses, therefore, the crossing of grain boundaries results in a lowering of the growth rate.

Figure 1.8 shows the typically observed behaviour of the crack growth rate with the explained effects at the grain boundaries.

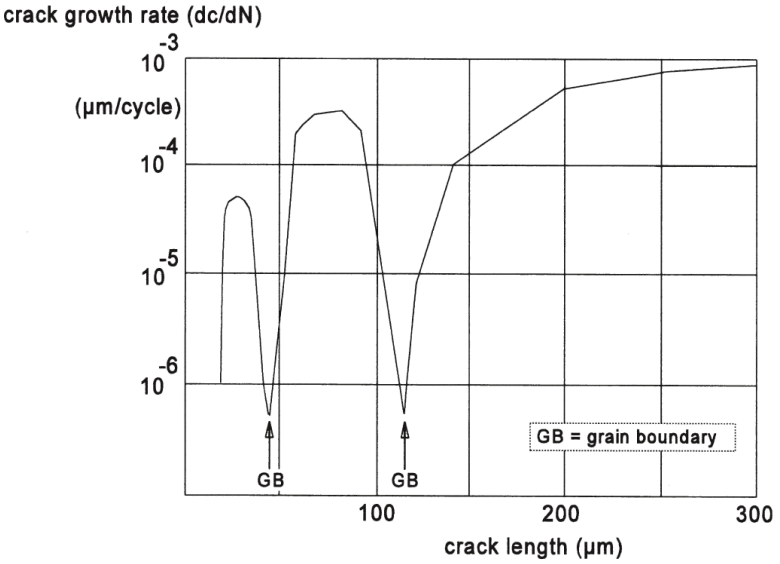

Figure 1.8: "Grain boundary effect on crack growth [...]."[17]

Furthermore, Figure 1.8 shows that for a large enough crack size the growth rate stabilizes and becomes a more or less continuous process. The cracks' growth rate is now defined by the so-called *crack growth resistance* of the material. Now the previously important surface factors roughness and favourable conditions for slip do not affect the process anymore. For the crack growth period, the following concludes:

"Crack growth resistance when the crack penetrates into the material depends on the material as a bulk property. Crack growth is no longer a surface phenomenon." [17]

In Figure 1.9 a few interesting aspects are illustrated. According to [17] the following facts hold:

1. Microcracks range down to less than $1\mu m$ for perfect surfaces but cracks which initiate at inclusions generally are of similar size as their starting inclusion. The only detectable sized cracks start from macro defects.

2. As shown by the two lower curves the crack is most of the time below $1mm$ in size and therefore practically invisible to the eye.
3. The two dashed lines are labelled as *non-propagating* cracks. In fact, not all cracks grow until failure.

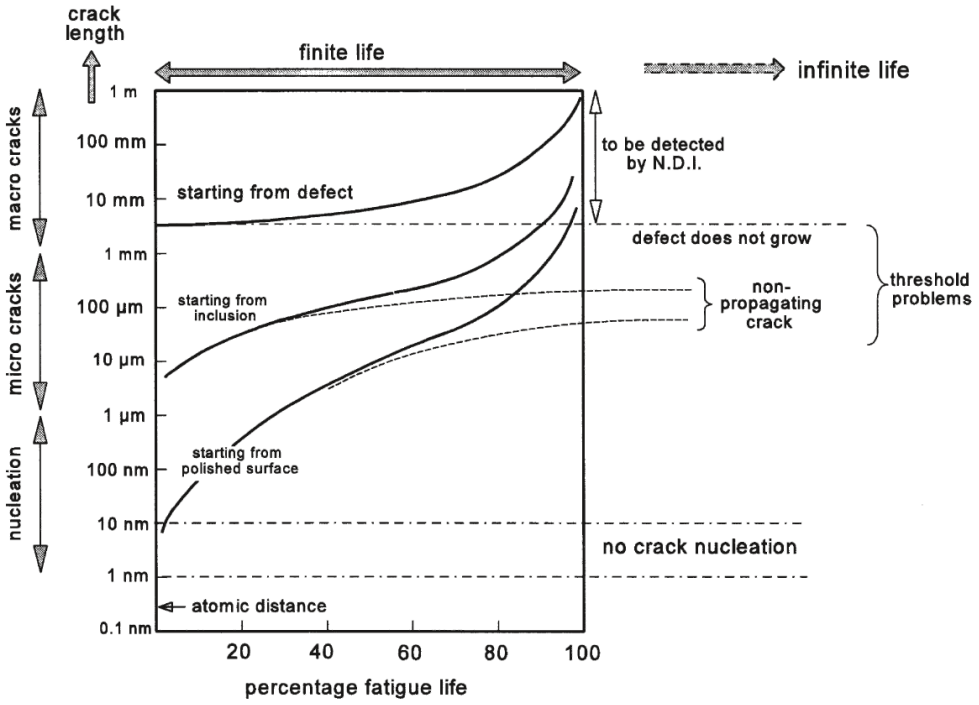

Figure 1.9: "Different scenarios of fatigue crack growth."[17]

Propagating and Non-Propagating Cracks

From both laboratory experiments and working environment observations, it has been shown that some initiated cracks do not grow past a certain size. Frost et al. [4] have found that for sharp notches with a large K_t, the crack initiation can not be avoided. Even for low stresses, due to the high-stress peaks, plastic deformation and crack nucleation occurs. However, it was also shown that the low-stress amplitudes were too low for continuous crack growth. Figure 1.10 on the next page displays these findings.

Furthermore, there is a possibility that a two-phased grain structure acts as a barrier for small cracks. For example, the α/β interfaces in Ti-alloys such as Ti-6Al-4V behave in such a manner. In general, the size of those non-propagating cracks are of comparable order as these *microstructural barriers* and therefore referred to as *microstructurally small cracks*.

Due to these non-propagating cracks, the fatigue limit can now be redefined

as the ”lowest stress amplitude for which crack nucleation is followed by crack growth until failure.”[17]

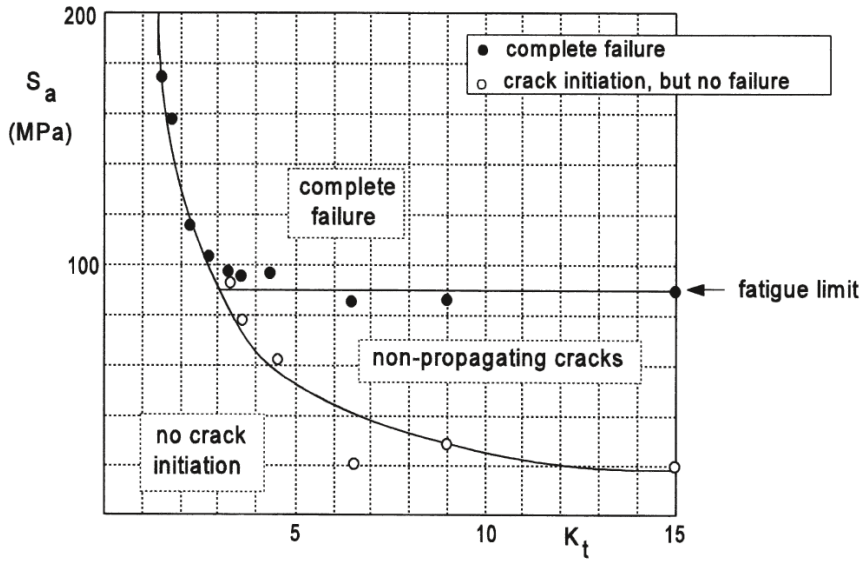

Figure 1.10: ”Observations [..] on non-propagating cracks as a function of K_t. Material: mild steel.”[17]

Chapter 2

Methods

2.1 Experimental Setup

2.1.1 Fatigue Testing

For the fatigue testing the so-called *strut* specimen were used. A strut is a micro testing specimen. They consist of a cylindrical bar in the middle, which is for a better usability connected to support structures on both ends. With these support structures, the sample can be clamped into the testing machine. For an increased stability of the sample, two supporting beams are printed along the middle part, which have to be removed (in our case cut) before starting the experiments. Figure 2.1 shows a Computer-Aided Design (CAD) realisation of the middle part of such a specimen.

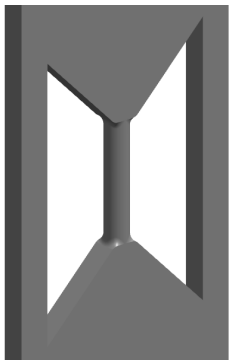

Figure 2.1: CAD image of a strut specimens' middle part.

Uniaxial fatigue tests were run with these strut specimen. In particular, all tests were conducted in *tension to tension* mode. This setup was chosen since tensile loads are known to be more critical for the fatigue performance compared to compressive loads. Furthermore, the propagation of cracks can be slowed down by compressive loads. This was observed with specimen which were examined under fully-reversed loading regimes that had a longer fatigue life compared to tension only tests. To further achieve a good comparability to the previous strut testing by the group and particularly D. Greenfeld [6], the same *stress ratio* of $R = 0.1$ was applied. Moreover, the same machine in the same *force-controlled* mode was used. All the tests were conducted with a *loading cycle frequency* of $f = 10Hz$.

The two pictures in Figure 2.2 show in *a)* the testing setup on the planar biaxial testing machine (MTS Systems Corporation, Eden Prairie, USA) and in *b)* a close-up picture of the clamping mechanism used to mount the strut specimen onto the machine.

For the tests, only one of the two axes, respectively two of the four hydraulic axes, were used. In particular, the axis number one and three, with number one used static and number three dynamically actuated. The load cell on axis one was used to measure the loads on the specimen to not include any inertia effects from the movement. The alignment of the two active axes is crucial for samples as tiny as our struts. That is why for each test close attention was paid on the orientation and the positioning of the specimen.

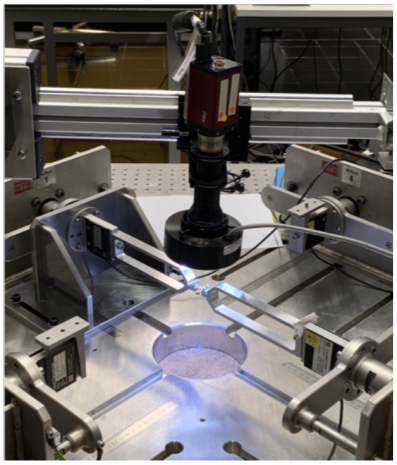

(a) Testing setup for struts on planar biaxial testing-machine.

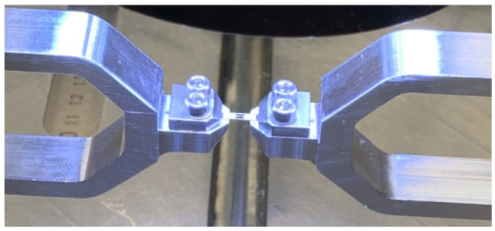

(b) Close-up of the clamping mechanism with a clamped strut specimen.

Figure 2.2: Testing setup for fatigue analysis of strut specimen.

All the tests were run in force-controlled mode, where the applied force levels were calculated from target stresses with respect to the cross-section of the nominal geometry A_{nom}. The loading-magnitudes were deduced from Daniel Greenfeld's [6] test results, which are displayed in Figure 2.3.

Two different diameters for the nominal geometry were examined to investigate a possible *size effect*. The following Table 2.1 lists the different applied stress levels during the experiments for both $200\mu m$ and $500\mu m$ nominal diameter struts. There were a total of fifteen experiments carried out, eleven for the $500\mu m$ and four for the $200\mu m$ specimen.

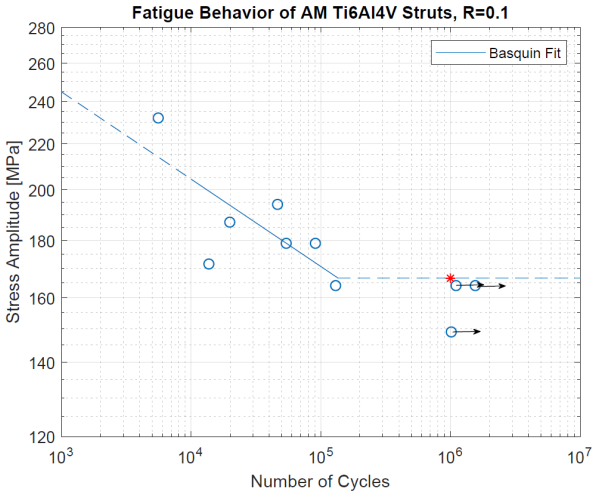

Figure 2.3: "S-N curve for AM Ti-6Al-4V struts."[6]

Table 2.1: Experimentally tested stress levels for 200μm and 500μm nominal diameter struts. Eleven tests with 500μm and four with 200μm were carried out.

nom Diameter in μm	Max Force in N	σ_a in MPa	σ_{max} in MPa	σ_{min} in MPa
500	78.54	180.00	400.00	40.00
	95.99	220.00	488.89	48.89
200	12.57	180.00	400.00	40.00
	21.00	300.80	668.45	66.85
	26.00	372.42	827.61	82.76
	25.00	358.10	795.77	79.58

2.1.2 Post Test Examinations

All the fracture surfaces of the tested strut samples were analysed with an optical microscope. The generated pictures were then further edited with the open-source image processing software *ImageJ* to calculate the value of the fracture cross-section area.

To this end the different pictures from the microscope were imported to the software and all consistently edited in the following order:

1. Import all the pictures from one sample as an *Image Sequence*. See Figure 2.4 (a).

2. Adjust the global scale to the scale on the microscope picture.
3. Convert the image to an 8-bit representation. See Figure 2.4 (b).
4. With the function *Convert to Mask*, the picture is transformed into an only black or white representation according to the chosen method. See Figure 2.4 (c).
5. Finally, the area is calculated with the function *analyse Particles*:
   a) Set the minimal particle size to 0.08 (if the Scale was set in *mm*).
   b) Toggle *Show Outlines*.
   c) Check *Display Results*.
   d) Confirm and run with *OK*.

With 5.a) an areal threshold for the smallest considered continuous details is defined. The final result of an exemplary picture can be seen in Figure 2.4 (d). The choice of which method is applied in the *Convert to Mask* menu mentioned above in point 4. was chosen visually to the best fit. This way, for each microscopic picture, a value for the cross-section is calculated and an average value can be determined for each strut sample.

In Table 2.2 the results for the area analysis with *ImageJ* are listed. The extreme values, however, have to be treated with caution. Since the measurement of the area highly depends on the pictures' focus. Furthermore, it is not recommended to try and draw any specific conclusions about the actual shape of the fracture area before testing from these pictures. The simple two-dimensional consideration is in this case not sufficient.

Table 2.2: Generated values for the fracture locations' cross-sections with ImageJ and their over- respectively undersizing in percentage to the nominal area. For comparison, the nominal value for the cross-section is $0.196 mm^2$.

Test #	Area in mm^2	Oversize in %	*Test #*	Area in mm^2	Oversize in %
Test_1	0.134	-31.6	*Test_7*	0.173	-12.1
Test_2	0.175	-10.9	*Test_8*	0.136	-30.6
Test_3	0.179	-8.8	*Test_9*	0.181	-7.8
Test_4	0.174	-11.2	*Test_10*	0.173	-12.1
Test_5	0.151	-22.9	*Test_11*	0.169	-13.9

The four pictures on the next page in Figure 2.4 show an exemplary *step-by-step* process from the microscope picture to a measurable outlined area.

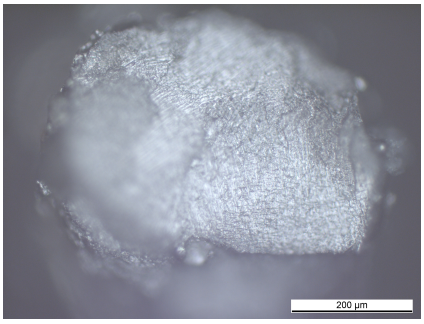

(a) Picture from the microscope

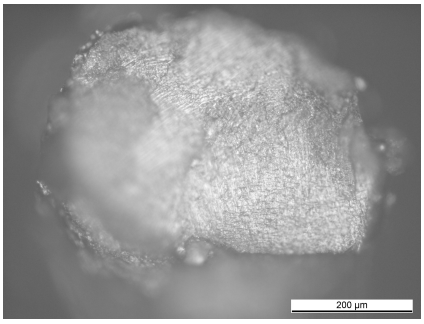

(b) After conversion to 8bit

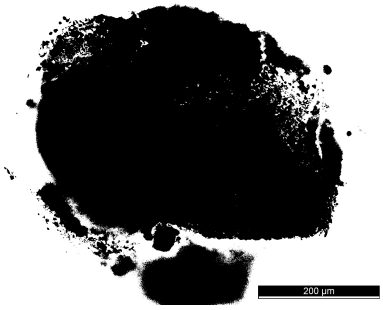

(c) After *Convert to Mask*

(d) Final generated outline.

Figure 2.4: Exemplary *step-by-step* procedure for an image post-process with the *ImageJ* software to analyse the real cross-section of a fatigue tested strut specimen at fracture location.

2.2 Theoretical Approach

As described in the Introduction chapter 1, stress concentrations are one of the main influences on a specimens' fatigue life during the initiation period. Especially the ones introduced by notches are common in the everyday use and work of engineers. Therefore they are thoroughly analysed and books such as Peterson's - *Stress Concentration Factors* [14] were put together full with formulas and tables to specify the K_t values for a given type of notch or for a given arrangement of notches.

2.2.1 2D Stress Concentration Factors

In the two-dimensional case considering *plane stress* or *plane strain problems*, the solution is for most real cases analytically solvable. The differential equations describing the system in equilibrium state are the three following ones from [18]:

$$\begin{aligned} \text{I} \qquad & \frac{\partial \sigma_x}{\partial x} + \frac{\partial \tau_{xy}}{\partial y} + \bar{p}_{Vx} = 0 \\ \text{II} \qquad & \frac{\partial \tau_{xy}}{\partial x} + \frac{\partial \sigma_y}{\partial y} + \bar{p}_{Vy} = 0 \\ \text{III} \qquad & \left(\frac{\partial^2}{\partial x^2} + \frac{\partial^2}{\partial y^2} \right) (\sigma_x + \sigma_y) = -f(\nu) \left(\frac{\partial \bar{p}_{Vx}}{\partial x} + \frac{\partial \bar{p}_{Vy}}{\partial y} \right) \end{aligned} \tag{2.1}$$

where $\bar{p}_{Vx}$ and $\bar{p}_{Vy}$ are the body forces per unit volume in the corresponding direction and f is a function of *Poisson's Ratio* ν:

$$f(\nu) = \begin{cases} 1+\nu & \text{for plain stress} \\ \frac{1}{1-\nu} & \text{for plain strain} \end{cases}$$

Additonally the surface conditions are:

$$\begin{aligned} p_x &= l\sigma_x + m\tau_{xy} \\ p_y &= l\tau_{xy} + m\sigma_y \end{aligned} \tag{2.2}$$

where p_x and p_y are the surface forces per unit area at the boundary in the corresponding directions. l and m are the directional cosines of the normal to the boundary.

For a constant body force distribution in Equation 2.1 III, the right-hand side reduces to zero. Under these assumptions, the analytical K_t can be calculated. Interestingly, with constant forces, the Equations 2.1 and 2.2 do not contain any material constants and therefore the values are only depending on the geometrical shape and loading conditions.

This property enables the use of other ways to experimentally estimate the stress concentration factor, e.g. with photoelasticity where a material is being used which differs from the actual structure of interest.[14]

2.2.2 3D Stress Concentration Factors

If the structure has to be considered as three dimensional, the calculation of K_t is not as evident as for two dimensions in Equation 2.1. Most stress concentrations are now also a function of the material constants. For many cases, the *Poisson's Ratio* is an important factor.

For the nominal strut structure of the tested specimen described in section 2.1.1, there is no exactly identical configuration to be found in [14]. The closest two are the ones to which the graphs for the values of K_t are shown in the Introduction chapter in Figures 1.2 and 1.3, where the structure is either considered to be made from a thin plate with a constant thickness or to be made from a round bar.

For the configuration at hand the formulas in the said figures leave the question open, as to what should be considered as the *unnotched* width H respectively diameter D. The three interesting configurations are the two extrema for both width and diameter and a chosen in between middle position, $Max = 1.5mm$, $Middle = 0.5mm$ and $Min = 0.275mm$. The maximal value corresponds to the outer thickness of the supporting structure in the strut samples and the minimal value to the nominal strut diameter plus two times half of the edge blend radius due to the 45° connection at that point. The calculated K_t values for the three positions are listed in Table 2.3.

Table 2.3: Values of the minimal and maximal calculated K_t for the nominal strut geometry under three different assumptions of D and H according to Peterson.[14]

D & H	Max	Middle	Min
in mm	1.5	0.5	0.275
max K_t	2.0	2.049	1.670
min K_t	1.421	1.8	1.352

The middle position was chosen such that the function describing the K_t-value in the case of a stepped tension bar of circular cross-section with shoulder fillet takes a maximum value. Therefore according to the theory, we would expect a K_t somewhere in the range between 1.3 and 2.1. This was used as an estimate to compare with the results from the simulations.

2.3 Paris-Erdogan Law For Strut Samples

As mentioned in section 1.3.3 Cracks, there are different types of cracks. If one plots the crack growth rate da/dN as a function of the stress intensity range ΔK for a certain material on a log-log scale it takes the characteristic form, as it is displayed in Figure 2.5 with its three main regions (I, II and III) and two vertical asymptotes. All values for ΔK outside and left of the *threshold region* I are too low and therefore irrelevant for crack growth. For all the values outside and right of the region III a direct complete failure is to be expected.

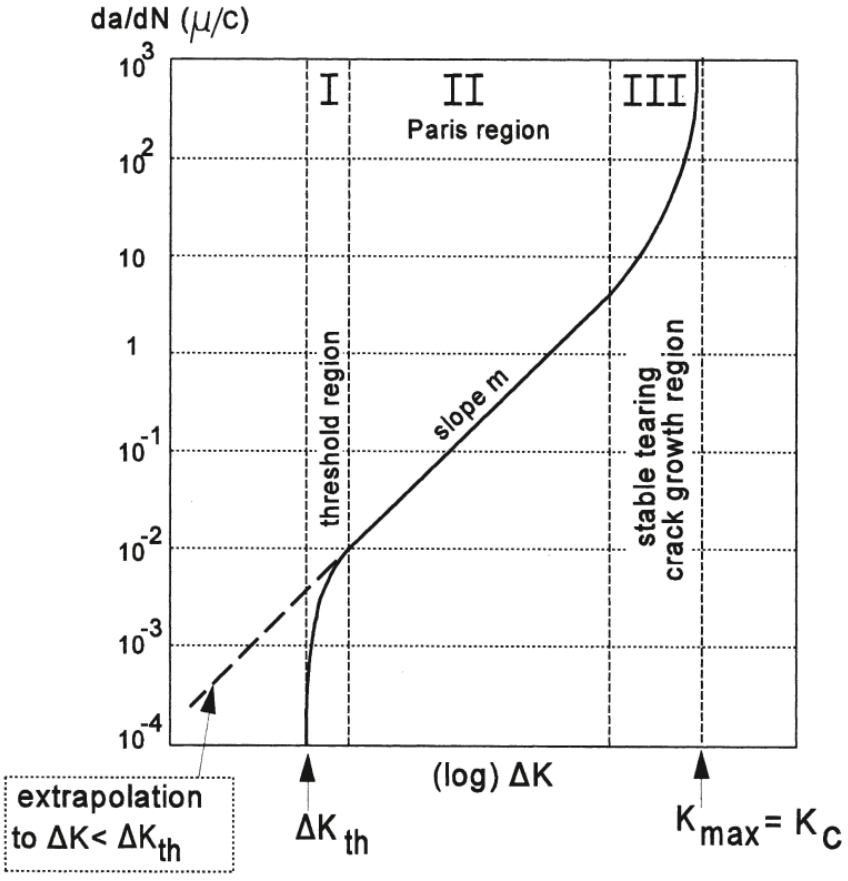

Figure 2.5: "Three regions of the crack growth rate as a function of ΔK."[17]

For the description of propagating cracks in the II region, the best-known equation is the so-called Paris-Erdogan Law [12]:

$$\frac{da}{dN} = C\Delta K^m = C\left(Y\Delta\sigma\sqrt{\pi a}\right)^m \tag{2.3}$$

With da: the infinitesimal change in crack length; dN: the infinitesimal delta in cycles and C, m: material parameters. The value for Y can be chosen equal to 1, which leads to an integrated form of Equation 2.3 that is analytically solvable for the number of cycles until failure N_f:

$$N_f = \int_0^{N_f} dN = \int_{a_0}^{a_f} \frac{da}{CY^m \Delta^m \sigma (\pi a)^{m/2}} = \frac{1}{CY^m (\Delta\sigma\sqrt{\pi})^m} \int_{a_0}^{a_f} a^{-m/2} da$$
$$= \frac{1}{C(\Delta\sigma\sqrt{\pi})^m} \frac{1}{m/2-1} \left(\frac{1}{a_0^{m/2-1}} - \frac{1}{a_f^{m/2-1}} \right) \tag{2.4}$$

where a_0 is the initial crack length and a_f the final one. For most classical materials the parameters C and m are listed in the book *Bruchmechanischer Festigkeitsnachweis für Maschinenbauteile: FKM Richtlinien*.[2] But for the case in this thesis with Ti-6Al-4V, there were no values to be found. In the dissertation of P. Huffman [7] the following plot, shown in Figure 2.6, can be found. They display the da/dN as a function of ΔK in log-log.

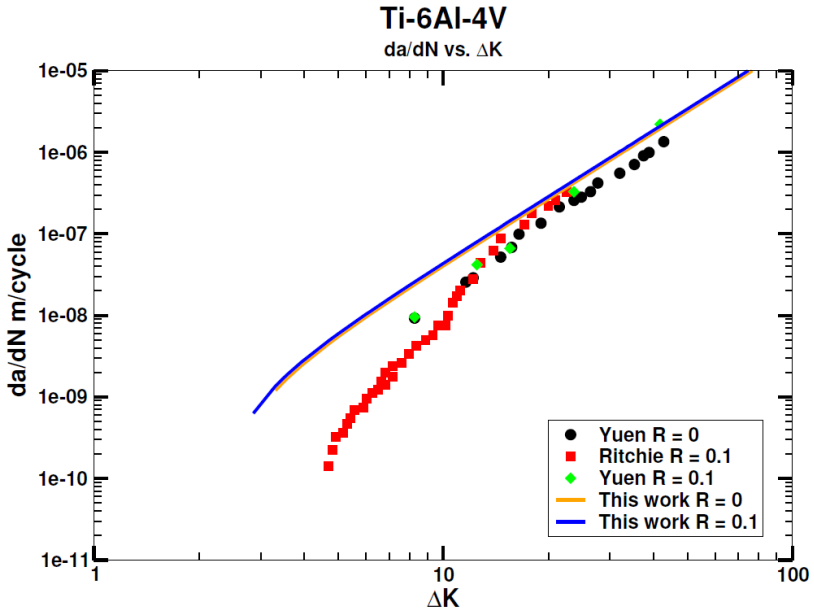

Figure 2.6: "Fatigue crack growth rate curves for Ti-6Al-4V at low-stress ratios[...]."[7]

Deduced from the plot the values for C and m for a stress ratio of $R = 0.1$ are the following:

Table 2.4: Values C and m for Ti-6Al-4V from Huffman [7].

C	m
1.97×10^{-10}	2.7

For the initial crack length a_0, the microstructure of the material has to be inspected. From the analysis with a Back Scattered Electron Diffraction (BSED) microscope pictures of the surface of specimen were generated, shown in Figure 2.7. The microstructure of AM Ti-6Al-4V is similar to the martensitic structure known from steels.

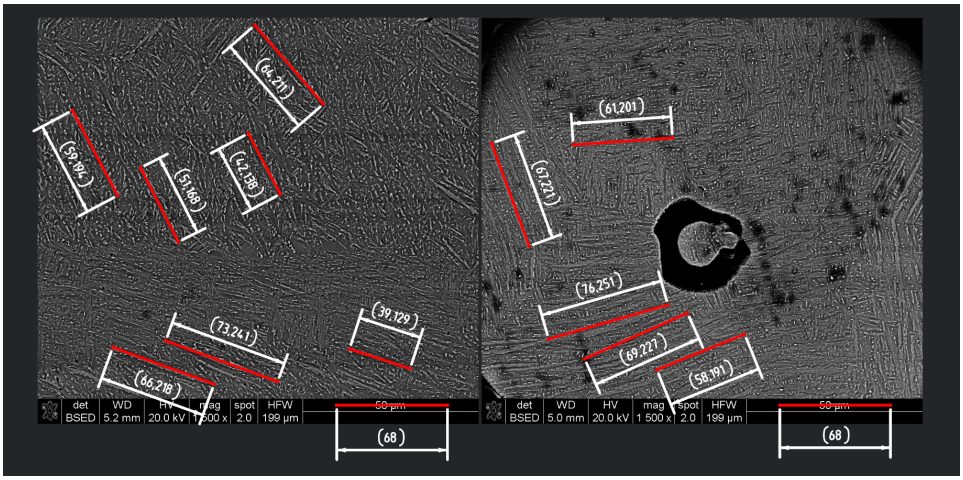

Figure 2.7: Microscopic pictures of struts with indicated lengths of the grain lentils diameters. All lengths with a scaling factor of 1.36 to large.

In the picture above all measured lengths are oversized by a factor of 1.36 due to picture scaling ($50\mu m \Leftrightarrow 68$). The measuring was done with *Siemens NX 11*. Since the martensitic lentils are a three-dimensional phenomenon the measured lengths have to be assumed as underestimating the maximal diameter. For the calculation of the initial crack length a_0, the average of the largest ten values was taken. This leads to an a_0 with the size of $0.0536mm$. If one compares this value to the calculated value from the *Kitagawa Diagram* in Figure 2.8 where $a_0 = 0.037mm$ it shows that this is larger than the minimal crack length.

Therefore we are in the field of elastoplastic fracture mechanics, where *Paris's Law* is technically not applicable. With this knowledge of discrepancy in mind here are the calculated values:

$$
\begin{aligned}
N_f(\Delta\sigma) &= \frac{1}{C(\Delta\sigma\sqrt{\pi})^m}\ \frac{1}{m/2-1}\left(\frac{1}{a_0^{m/2-1}} - \frac{1}{a_f^{m/2-1}}\right) \\
&= \frac{1}{1.9\times 10^{-10}(\Delta\sigma\sqrt{\pi})^{2.7}}\ \frac{1}{0.35}\left(\frac{1}{0.2^{0.35}} - \frac{1}{0.05361^{0.35}}\right) \\
&= \Delta\sigma^{-2.7}\ 3.699\times 10^{10}
\end{aligned}
$$

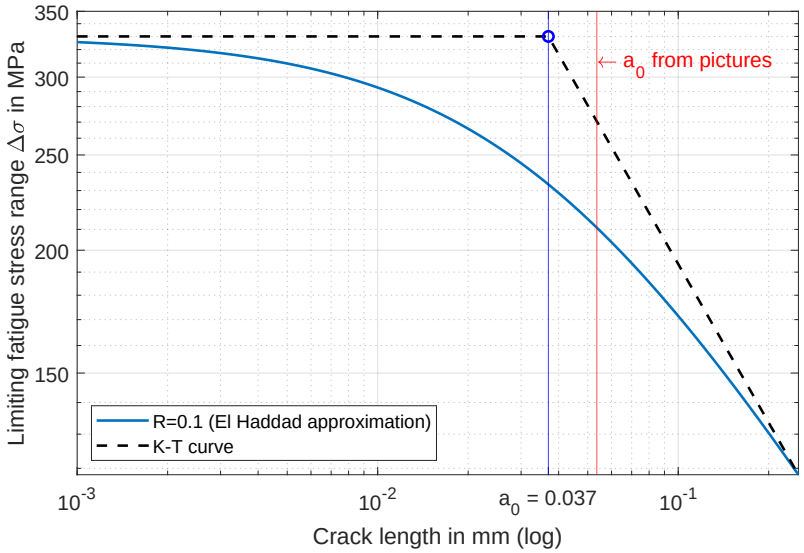

Figure 2.8: Calculated *Kitagawa Diagram* for AM Ti-6Al-4V with values from Greenfeld [6] and the formulas for the curves from the FKM Richtlinien [2].

With this formula, one can approximate an *S/N-Curve* shown in Figure 2.9, where for comparison the experimental results of D. Greenfeld [6] and the values for machined Ti-6Al-4V from Li et al [8] are displayed as well. From the graph, we see that for lower values of ΔS ($\Delta S = 2 * \sigma_a$), the calculated prediction of the *Paris Erdogan Law* is diverging from the measured values. The reasons for that are amongst other things the following:

- The problem is *crack initiation dominated* and therefore the more relevant portion of the fatigue life is until the crack reaches the critical crack length. In Equation 2.4 the integration starts from an initial crack length which is equal to a_0. Thus it completely disregards the initiation timespan.
- The *Paris' Law* is not applicable according to the calculation of the *Kitagawa Diagram* as introduced in the FKM Richtlinien.[2] According to

them, the problem lies in the regime of elastoplastic fracture mechanics.

- The used parameters from [7] are derived for machined traditional Ti-6Al-4V and might be inaccurate for our material.
- It is never possible to predict the fatigue limit with the *Paris Erdogan Law*.

Overall the results are as it was expected and within the known limitations to the applicability of the law.

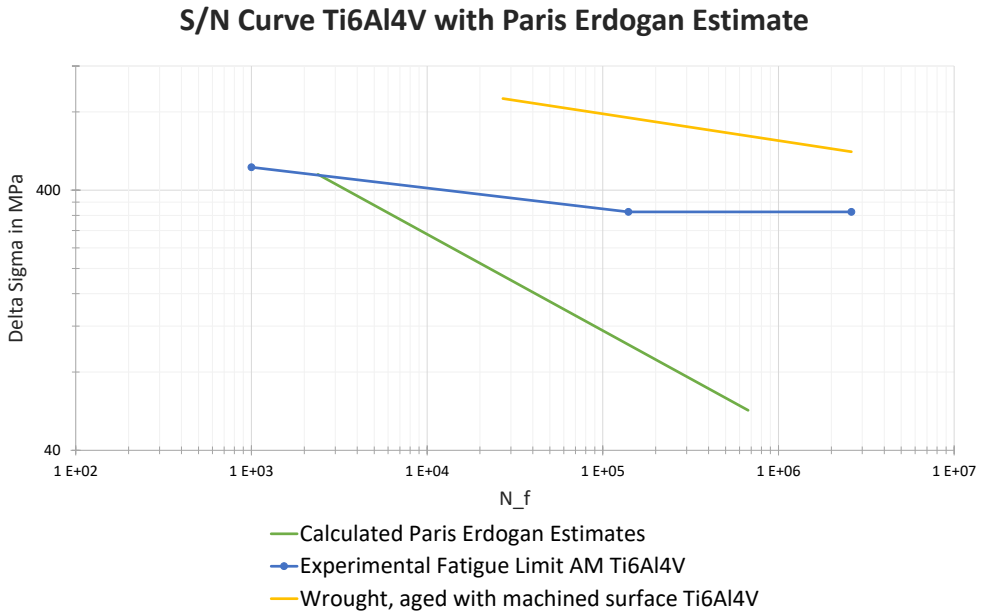

Figure 2.9: Calculated *S/N Curve* from the *Paris Erdogan Law* 2.3. For comparison, the measured data form Greenfield [6] for AM struts and the data for traditionally manufactured Ti-6Al-4V from Li et al [8].

2.4 FEA Approaches on Nominal Strut Structure

The idea was to calculate the value of K_t for the nominal structure of our strut specimen. The underlying geometry to the following FEAs is shown on the right in Figure 2.10. An edge blend with a radius of $R = 0.075mm$ connects between the cylindrical strut and the 90-degree angled flat section. For the nominal geometry, the maximum stresses are expected in the root of this mentioned edge blend. With the *Simulia Abaqus CAE* software, the part was meshed and the load case was introduced. The lower rectangular face (respectively to the positive z-direction) was set to be fixed with the corresponding boundary condition (BC) and on the upper one, the load was applied with a negative valued uniform pressure.

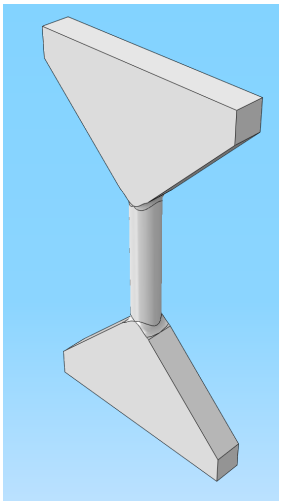

Figure 2.10: 3D geometry in Abaqus for the nominal strut FEA.

Since the whole simulation is evaluated only linearly, the calculated value for K_t is independent of the magnitude of the stress used. This simplification is valid since the fatigue limit is for most materials at around $0.2 * R_{p0.2}$ and for these stress levels, the assumption of linear behaviour according to *Hooke's law* is a good enough approximation.

2.4.1 FEA Setup on Nominal Structure

For the previous experiments on the strut samples, the fatigue limit was determined at an amplitude σ_a of roughly 165 MPa for a stress ratio $R = 0.1$ (tension to tension). To get from the amplitude to the maximal and minimal stresses σ_{max} and σ_{min} respectively, one uses the following relations:

$$0.1 = R = \frac{\sigma_{min}}{\sigma_{max}} = \frac{\sigma_m - \sigma_a}{\sigma_m + \sigma_a} \quad \Rightarrow \quad \sigma_a = \frac{1}{2}\left(\sigma_{max} - \sigma_{min}\right) = \frac{1-R}{2} * \sigma_{max}$$

$$\Rightarrow$$

$$\sigma_{max} = \sigma_a * \left(\frac{2}{1-R}\right) = 165MPa * \left(\frac{2}{0.9}\right) \approx 366.7MPa$$

$$\sigma_{min} = \sigma_a * \left(\frac{2 * R}{1-R}\right) \approx 36.67MPa.$$

where σ_m is the average stress for the loading cycle. To derive the pressure on the upper surface of the geometry that leads to the wanted σ_{nom} in the circular section, the aimed for value was divided by the area ratio R_{Area} of the

cross-sections (top surface to the middle cross-section of nominal geometry):

$$R_{Area} = \frac{A_{top}}{A_{middle}} = \frac{1.5mm * 0.2mm}{(0.1mm)^2 * \pi} = 9.5493.$$

In our case, the stress level aimed for at the nominal cross-section, was the experiments maximal stress at the fatigue limit $\sigma_{max} = 366.7MPa$. From this the equivalent load σ_{top} was deduced to:

$$\sigma_{top} = \frac{\sigma_{max}}{R_{Area}} = \frac{366.7MPa}{9.5493} = 38.401MPa.$$

In Abaqus, the simulation with the above-derived stress was then repeated for different mesh sizes. For each refinement the mesh was set up according to the following 5 steps:

1. Seed the part to the minimum wanted mesh size.
2. With seed edges apply the rough outer mesh on the cubical outmost parts with mesh size $0.1mm$.
3. For the 45° angled connecting edges from the cubical to the cylindrical region set a one directorial (single) bias from $0.1mm$ to the minimum wanted mesh size.
4. Define the number of knots on the edges before the edge blend as fixed to the minimum mesh size and the amount as unchangeable.
5. Generate the mesh.

The mesh refinement aims to quantify the K_t value for its mesh dependency and to investigate a convergence in simulation results.

2.4.2 One Per Cent Approach

From the article [9] we got the idea to use what we called the *one per cent approach* for the K_t approximation. Instead of taking the obvious choice for the maximal stress value and simply taking the maximal calculated value from the simulation, the suggestion is to take an average stress value for the top 1% of generated values. The argument behind this approach is that finite element methods tend to result in unrealistic singularities within the stress field due to distorted mesh elements. This leads to overshoots in the calculated simulation results.

After assessing the method and giving it some deeper thought it was concluded to not follow down this path any further because of the following unwanted properties of the method:

- Let us consider a given notched geometry, for which the *correct* value for K_t is known, such as a semicircular groove in a cylinder. From the

chart 2.19 out of Peterson's *Stress Concentration Factors* [14], we get a specific value in the range of 1.7 to 3.1 depending on the ratio between the radius r of the grove and the diameter D of the cylinder r/D and no other influences.
But for the method at hand, our value for K_t mostly depends on the size of the cylinder around the groove. The more material is represented in the simulation, the further away from the notch spreads the range of considered elements for the 1% highest values. Thus lowering the average value through obvious reasons. This behaviour leads to a complete dependency on meshing and on the design of the simulated structure with less importance for the notch itself. Furthermore, the comparability of different geometries with different meshes is impossible.

- The argument that FEA simulations have singularities at which the stress values overshoot largely is valid. These problems tend to occur at locations where one either expects them (e.g. sharp edges) or at locations where one knows that no such stresses will occur (e.g. edges and boundaries with connections to the simulations' BCs).
  These problems are possible to be averted by introducing edge blends (that normally also represent the real case more exactly, since the perfect edge from manufacturing does not exist) or simply to disregard of such single nodes, where overshoots occur.

2.4.3 Maximal Absolute Principal and Maximal Mises Stresses

Intuitively one would compare the simulations' maximal value to the calculated nominal value, which was done in choosing the *Maximal Principal Stress* and the *Maximal Mises Stress* to derive two values for K_t. The difference between the two lies of obviously in their calculation.

The *Maximal Principal Stress* is obtained by calculating the stress tensor's eigenvalues and taking the one with the largest absolute value. This leads to the maximal occurring stress in the whole body.

The *Maximal Mises Stress* however, is calculated by the well known formulas:

$$\sigma_{v,M} = \sqrt{\frac{1}{2}\left((\sigma_{11}-\sigma_{22})^2+(\sigma_{22}-\sigma_{33})^2+(\sigma_{33}-\sigma_{11})^2+6(\sigma_{12}^2+\sigma_{23}^2+\sigma_{13}^2)\right)} = \sqrt{\frac{1}{2}\left((\sigma_1-\sigma_2)^2+(\sigma_2-\sigma_3)^2+(\sigma_3-\sigma_1)^2\right)} \tag{2.5}$$

where the symmetric stress Tensor $\boldsymbol{\sigma}$ is equal to $\boldsymbol{\sigma} = (\sigma_{i,j})_{i,j=1}^{3}$ and $\{\sigma_i\}_{i=1}^{3}$ represent the three principal stresses. This reduces the maximal value by the

amount of *hydrostatic pressure*. It is a commonly used measure for ductile materials.

With the two values for maximal stress, two K_t values are generated due to comparison to the same nominal stress. This gives a certain bandwidth where the *real* value can be expected, for a more conservative approach the larger of the two should be chosen.

2.4.4 FEA Approach on Size Effect for Nominal Struts

The size effect of the nominal geometry was FE analysed for different strut diameters. In particular the diameters $d = 200\mu m$, $300\mu m$ and $500\mu m$ were simulated. To all geometries, the same edge blend was introduced with a radius of $R = 0.075mm$ as described in the first part of chapter 2. The loads to the geometries were calculated in the same way as in section 2.4.1 such that for all sizes σ_{nom} was equal to $366.7MPa$. In that way, all the K_t calculations were with the same σ_{nom}. If the same theory as described in section 2.2.2 is applied to all three diameters, then Table 2.3 can be expanded to the following more comprehensive one:

Table 2.5: Table with the minimal and maximal calculated values K_t for the nominal strut geometry according to Peterson [14] for the three different strut diameters $200\mu m$, $300\mu m$ and $500\mu m$.

	$200\mu m$			$300\mu m$			$500\mu m$		
D & H	Max	Mid	Min	Max	Mid	Min	Max	Mid	Min
in mm	1.50	0.30	0.075	1.50	0.80	0.375	1.50	0.80	0.575
max K_t	2	2.05	1.67	2.1	2.1	1.63	2.4	2.16	1.61
min K_t	1.42	1.8	1.35	1.58	1.83	1.42	1.8	2	1.51

It showed that for the bigger diameters, the stress concentration should increase. This was as expected since the edge blend radius stays the same while the diameter increases, which is a comparable effect to reducing the radius for a constant diameter. For the value of K_t, the relation between diameter and radius is relevant. Thus the larger the diameter, the more the constant edge blend size acts like a sharp edge and less like a continuous blend and therefore K_t rises.

The three nominal geometries were all simulated with different mesh sizes analogue to the described case of the $200\mu m$ as explained in section 2.4.1.

2.5 FEA Approach on The Real Structure

After the FEA of the *nominal strut geometry,* the next task was to analyse the real AM structure. Thanks to the previous work of S. Robmann [15] there were already as STL-files exported micro Computer Tomography (μ-CT) scans of struts available. An example is shown in Figure 2.11.

Figure 2.11: μ-CT scan converted to STL-file of an AM Ti-6Al-4V strut with $200\mu m$ nominal diameter (strut *S1_4_1*).

2.5.1 Steps from STL to Abaqus

A few post scanning modifications had to be done to the scan created STL-files. The biggest change was to construct additional material onto the top and bottom of each strut to apply BC's and loads. Working with STL-files is tricky since the files are neither simple to work with nor are they easily transformed into other better usable formats. This is due to the minimized amount of information stored in the files themselves caused by the triangulated representation.

The finally chosen approach to adjust the files and import them into Abaqus was the following:

1. Import STL-file into *Siemens NX 12* as a convergent body.
2. Move the created body into the part origin.
3. Sketch additional geometry in the *x-y plane* and extrude symmetrically the top and bottom parts.

4. Mesh generation in NX:
   a) Start a *new FEM and Simulation* with the *Pre/Post* application.
   b) Create no idealized Part, use *high* for the *Polygon Body Resolution* and choose *Abaqus* as Solver in *Solver Environment*.
   c) Mesh the geometry to the desired mesh.
   d) *Activate Simulation*.
   e) Export to Abaqus under *File* → *Export* → *Simulation*, select to output only *Nodes and Elements* under *Output Options* choose filename and export directory and generate the *inp - file*.
5. Import part to Abaqus from the created file under *File* → *Import* → *Part*.

At this point, it has to be highlighted that this was the only process, which turned out to be fruitful for some of the μ-CT scanned STL-files. I could not find a process that enabled me to generate the desired fine meshes for all the samples. On the contrary, even this method only worked for a few scans.

2.5.2 FEA Setup for Real Struts

Upon including the *Siemens NX* mesh into Abaqus the FEA can be set up the same way as for any other geometry of course without the need to generate a mesh. For the simulations' setup the following settings were chosen:

- Material *AM Ti-6Al-4V* as elastic and isotropic with *Young's Modulus* of $100GPa$ and a *Poisson's Ratio* of 0.25.
  The value for the *Young's Modulus* is not as critical to be 100% accurate since the load is introduced as force and not displacement and we only care for the quantitative results in stress but not strain.
- A *Reference Point* above the top surface was introduced.
- The top surface mesh nodes were connected by a kinematic coupling constraint where all degrees of freedom were included. Like this, the whole surface displaces by the same vector as the reference point does.
- The load was calculated such that the force would generate a σ_{nom} equal to the $\sigma_{max} = 366.7MPa$ from the experimental fatigue limit which results in a force of:

  $$\sigma_{nom} = \frac{F}{A_{nom}} = 366.7MPa \Rightarrow F = \sigma_{nom} * A_{nom} = 11.5202N$$

  which was applied in the vertical direction at the *Reference Point*.
- Two BC's were included:

- The lower mesh surface to be fixed in all degrees of freedom.
- The reference point to be fixed in all degrees of freedom but the direction of the force.

For faster solving of the FEA, the added geometries are meshed coarse with the *Mesh Control* functions in *Siemens NX*. An example of a meshed real strut is shown below in Figure 2.12. As explained in the last point above its BC's are highlighted with blue and orange wireframe cones visualizing the fixed constraints for rotation and displacement.

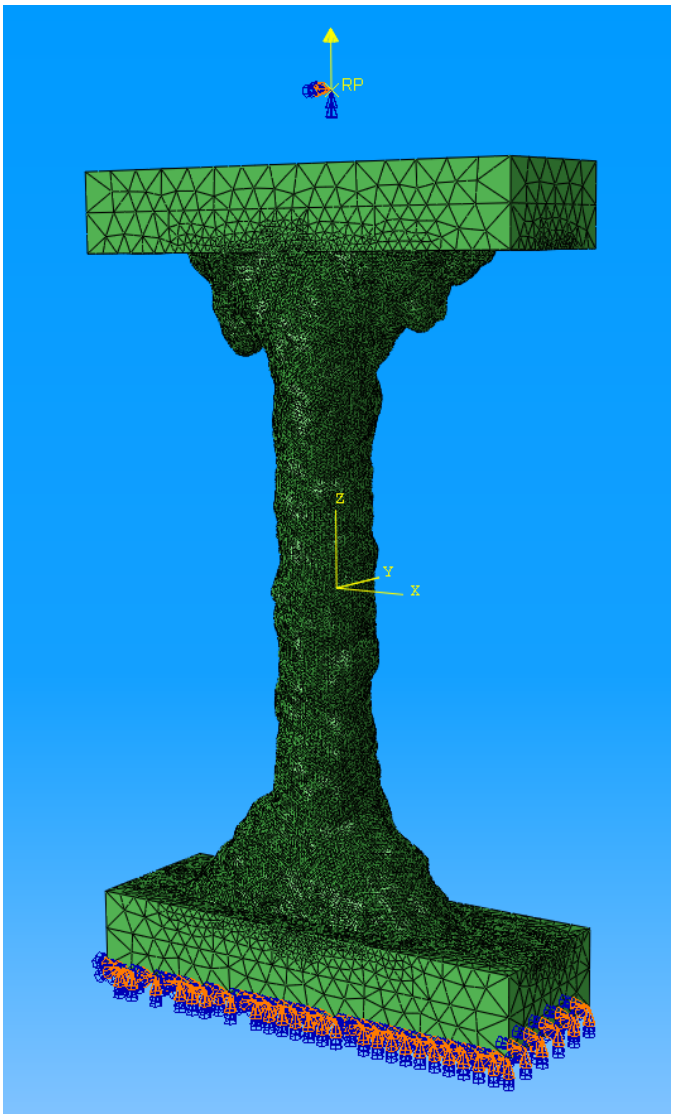

Figure 2.12: Abaqus FEA setup for *real strut geometry* with visualized BC's and load on *Reference Point* (strut *S1_4_1* with 0.0125*mm* mesh size).

Chapter 3

Results and Discussion

3.1 Experimental Results

3.1.1 Expected Results

The expectations before starting the experiments were that there should be a size effect and that it should be the $500\mu m$ diameter struts, which are more resistant to fatigue stresses. The initial idea was that the governing characteristic to the determination of the fatigue life was to be found in the geometry mismatch from the AM process. Since this is an absolute value (the accuracy of the printer), the smaller the sample the larger the relative error and vice versa. The fabrication details for the tested strut samples are the following:

"An AM250 system, a laser power of 200 Watt, and Ti-6Al-4V powder were used. The powder was plasma-atomized to obtain a particle size of $14 - 45\mu m$. The layer thickness of the powder bed was $30\mu m$. All specimens were annealed at $850°C \pm 10°C$ for 2 hours. No surface treatment and no hot isostatic pressing (HIP) treatment were performed."[5]

Meaning that for our strut samples the worst case in smallest particle size was roughly 22.5% of the nominal diameter for the case of $200\mu m$ struts and 9% for the $500\mu m$ ones. From these numbers and from optically visual geometry faults on the printed samples the above described assumption arose. To have the maximal possible size effect in the experiments and due to time limitations, only the thinnest the $200\mu m$ and the thickest the $500\mu m$ printed struts were tested.

3.1.2 Fatigue Testing Results

Cross-Section and Stress Calculation

All the experimental tests were run in force-controlled mode, meaning that the stress levels have to be calculated under the assumption of a certain cross-section. Within this decision - how to specify the cross-section - lies the challenge. For best usability from a design point of view for a first approach, the nominal geometry was chosen. The aim was to have results, which would give factors that could directly be used together with the dimensions in CAD and thus would be simplest to implement. Therefore the first approach was to calculate the stress levels using the theoretical geometry. Which leads to $0.196mm^2$ for the $500\mu m$ and $0.031mm^2$ for the $200\mu m$ struts.

The results from the fatigue tests, however, showed an interesting distribution. Mainly the smaller struts performed unlikely well, e.g. a runout occurred at $\sigma_a = 372.42MPa$ with σ_{max} equal to $827.6MPa$ and σ_{min} respectively to $82.76MPa$, which would be an extraordinary fatigue performance if one considers the yield strength of roughly $900 - 1000MPa$ according to [13]. The plot below in Figure 3.1 shows the generated data with the stress values calculated according to the cross-section of the nominal geometry.

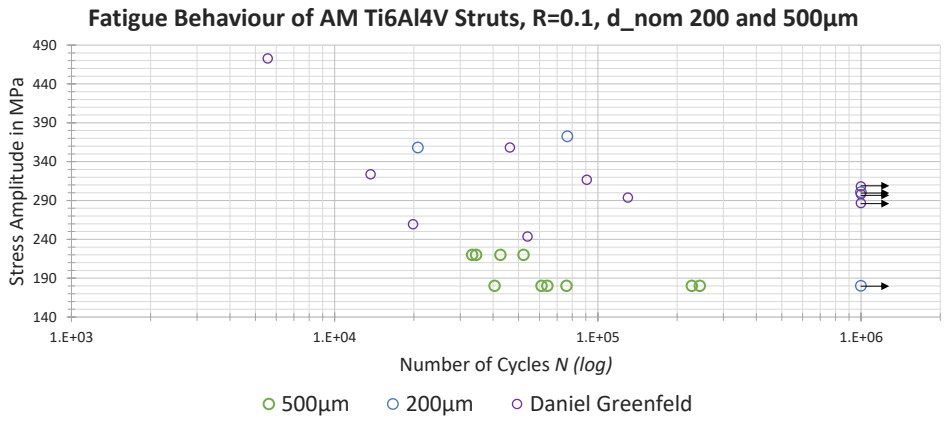

Figure 3.1: The experimental results of the fatigue tests considering the nominal geometry for the stress values. Results from [6] are converted to the same calculation from the given testing forces used for his testing.

The data in Figure 3.1 suggests clearly that the $500\mu m$ struts perform inferior to higher stresses than the smaller $200\mu m$ ones. This was not as expected and further investigations into the actual cross-section of the specimens were conducted.

A second and different approach to calculate the considered nominal cross-section was made. In previous work by D. Ghedalia [5] amongst other things, an oversizing factor for the different strut diameters was found. Table 3.1 lists the values for vertically printed strut samples and the in Table 3.2 the area for the nominal vs. the corrected cross-sections are specified. These values come from analysing the struts' dimensions. Which were measured from optical microscope images. Therefore this is a two-dimensional approach, for which the transformation into the three dimensional oversizing is under the assumption of circular cross-sections. For the final oversizing factor an average over several measurements was taken. The real geometry, however, must not be as simple as S. Robmann showed in his work.[15] His example of a horizontally printed strut (on page 29) shows that the deformation due to oversizing and miss printing is possible to be a largely varying phenomenon along the struts middle part. Therefore taking the average is risky and not in all situations appropriate.

In our case, however, where only vertically printed specimens were looked at, considering the average diameter is a valid approach. This is due to the *least-waviness* and *smallest geometry mismatch* in vertically printed specimens compared to other printing directions. A clear tendency for the waviness factor is that it decreases the closer to vertical the printing direction is, e.g. for $500\mu m$ struts it is at 7.99% for a horizontal printing direction and decreases monotone to the minimal value of 4.28% with vertical direction.[5]

Table 3.1: Oversizing factors for vertically printed strut samples from Daniele Ghedalia.[5]

nominal diameter	$200\mu m$	$300\mu m$	$400\mu m$	$500\mu m$
oversizing in diameter	1.53	1.36	1.17	1.14
oversizing in area	2.34	1.84	1.36	1.3

Table 3.2: Nominal cross-sections vs. corrected cross-section with oversizing factors from [5].

in mm^2	$200\mu m$	$300\mu m$	$400\mu m$	$500\mu m$
nominal cross-section	0.0314	0.0707	0.1257	0.1963
oversized cross-section	0.0735	0.1301	0.1709	0.2553

With these area-corrections, the experimental results take a new shape and

arrange more the way it was expected. This can be seen in Figure 3.2. It shows that if the AM oversizing is taken into account, the two types of struts arrange such that the original expectations look more likely. Due to the bigger size of the struts, the absolute printing error becomes relatively smaller than for the thinner ones. The difference is visible.

An even further refinement in the calculation of the real cross-section was the post-testing analysis of the final fracture area of each strut with an optical microscope and calculation of its area. The step-by-step process was further described in section 2.1.2. It is clear that also for this method some limitations in terms of accuracy exist. But the approach to look at the fracture location's cross-section is a more reasonable approach than simply taking a rather arbitrary average over different measured cross-sections, since the geometry mismatch is a very specimen specific effect.

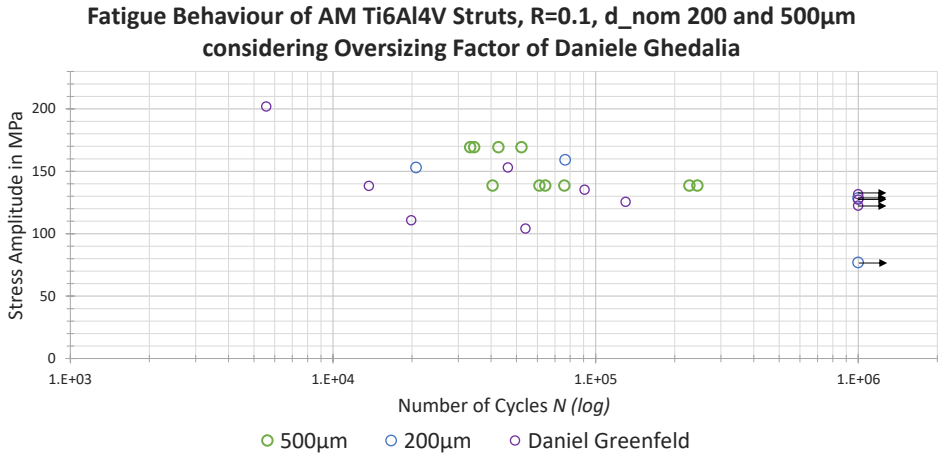

Figure 3.2: The experimental results of the fatigue tests considering the oversizing as described in [5]. Results from [6] are converted to the same calculation from the given testing forces used for their testing.

The approach to look at the fracture location is interesting and valid as this is the area where the maximal stresses occurred during testing. It is the location where the optimal conditions for crack initiation and growth lay. Meaning a maximum of superposed properties like a small cross-section to increase the overall stresses on the section or the presence of a strong notch (with a large K_t) that induces a high stress concentration. Another big influence can be the presence of structural printing defects such as air bubbles trapped in the material. For these reasons, the fracture area is always an interesting surface to analyse and measure for a reference area to calculate the nominal stresses.

One of the problems with analysing the fracture surface is that the final rupture is always coupled with plastic deformation and necking due to the very small remaining cross-section that induces high stress values. Thus the final fracture area is normally plastically deformed and if measured the area is smaller than before testing. With the knowledge of these limitations, the argument for this method is that the measurements are still closer to the relevant cross-section for our struts compared to the already discussed average. Due to the considerable waviness of the middle part in the strut samples, the cross-sections taken for the average tend to oversize the wanted area.

If only the $500\mu m$ struts are considered and the stress levels according to the different calculation methods are plotted, the results are as shown in Figure 3.3. Interestingly the analysis of the fracture area shows no oversizing but rather an undersizing of the local cross-section. For the $200\mu m$ only two samples were tested and the cross-section analysed. For these two samples, the analysis showed a clear oversizing slightly below the values of [5].

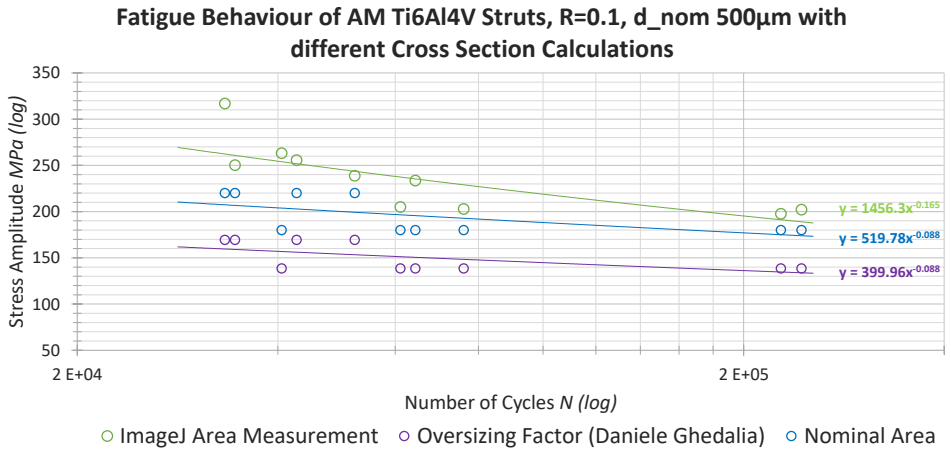

Figure 3.3: Fatigue test results for $500\mu m$ struts with the three different area calculation methods, nominal area, oversizing factor according to [5] and analysis with microscope and ImageJ of the fracture surface.

For a final comparison of the two specimen sizes' fatigue performance in Figure 3.4, the data is plotted in log/log. This time the stresses are calculated with the measured fracture areas for the $500\mu m$ diameter struts. From this plot, a size effect can be deduced. If the relevant cross-section for the real stress is measured the $200\mu m$ no longer outperform the $500\mu m$ but rather succumb to the printing limitations of SLM AM. For each size, a power trendline is drawn for each one the equation is shown.

To conclude, as it was expected there is a size effect which makes the thinner specimen prone to fail earlier than the bigger ones. This effect, however, is only visible if the real cross-sections are analysed. The oversizing problem with the $200\mu m$ struts completely dominates all other effects. It produces the largest influence on the behaviour of the struts such that the target of a globally valid K_t factor could not be reached for a range of different nominal cross-sections. The problem at hand has too many manufacturing process-specific parameters that influence it.

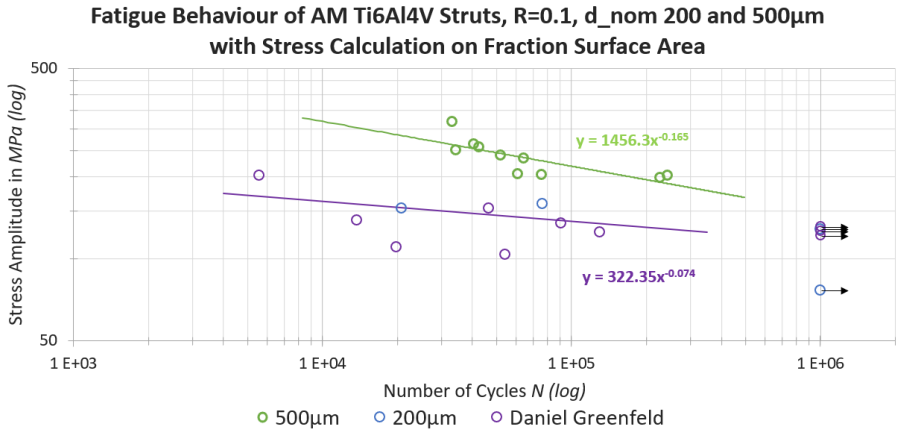

Figure 3.4: Fatigue test results for $200\mu m$ and $500\mu m$ with data from [6]. The power trendlines for both sizes are excluding the runouts. For the $500\mu m$ specimens, the stresses were calculated using a light microscope and the software ImageJ to measure the fracture surface as reference area and for the $200\mu m$ the oversizing factor from [5] was used to modify the nominal diameter.

Fracture Locations

In the previous experiments by the group, the observation was made that the specimens mostly fail at the connection between the middle part and the bigger supporting structure. Also for the new additional tests, this was an overwhelming trend. All the struts broke at either one of the two ends, where the cylindrical part changes into the angled flat supporting structure. In Figure 3.5 a histogram with the distribution of the fracture location is shown:

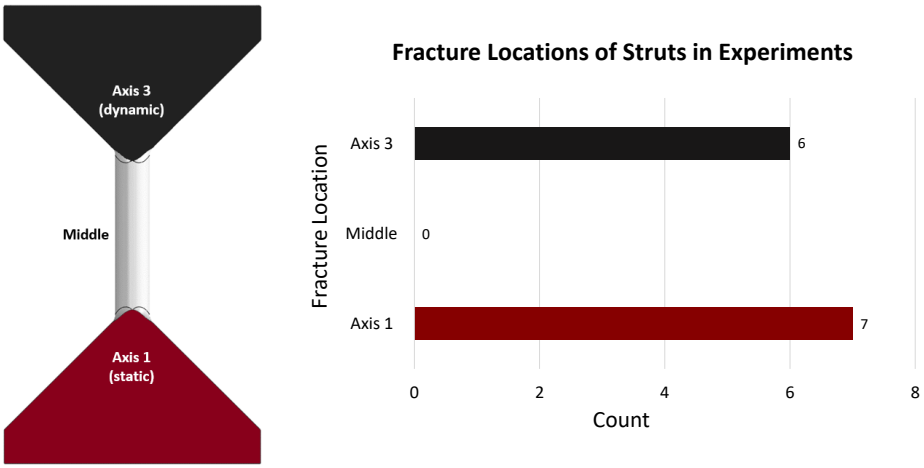

Figure 3.5: Fatigue test fracture locations of the strut specimens. All the struts broke at either one of the two ends, where the cylindrical part changes into the angled flat supportingstructure.

It is not completely clear what causes this phenomenon. Two approaches to explain are as follows:

1. The alignment as shown in Figure 2.2 (b) in the machine is never perfect to the last decimal. It has to be set optically and was done to the best of my capabilities. But there remains an uncertainty how close to the theoretical perfect alignment the machine was. To quantify the effects a short back-of-the-envelope calculation was made. It showed that the effect of induced stresses due to misalignment showed is not negligible at all. For the $500\mu m$ struts, it resulted in a difference of roughly 15% and for the $200\mu m$ with the consideration of oversizing roughly 22%.

2. The nominal geometry of the strut induces with its shape a stress concentration at the exact location where the probes fail.

Of course, both effects are very likely to be superposed.

Regarding point 1: If there were a slight misalignment, then there was additional unwanted induced bending on the specimen, which influences the testing conditions largest at the ends of the middle part, where the clamping mechanism fixes the two sides. E.g. a short conservative back-of-the-envelope calculation for an assumed misalignment of $0.05mm$, the additional imposed stress would be roughly 70-80 MPa for the oversized $200\mu m$ nominal strut. This results if the middle section is simplified as a one side clamped cylindrical beam. For the hand calculations and an additional FEA see Appendix A.

Regarding point 2: For a further analysis of this effect, the effort to analyse the structure with FEA was made. Its results are discussed in section 3.2.

Another interesting fact was that for nine out of thirteen test specimens there were well visible air inclusions in the fracture surface, which also function as considerable notches *(spherical cavity in an infinite body* $\rightarrow K_t = 2.05$ *from [14])*. Figure 3.6 below shows a few of the fracture surfaces with clearly visible inclusions.

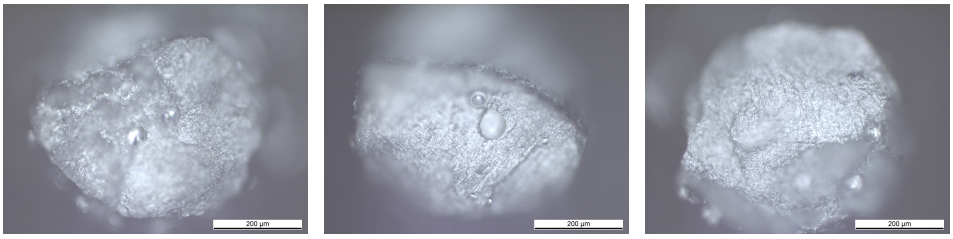

(a) Test 7 (b) Test 8 (c) Test 1

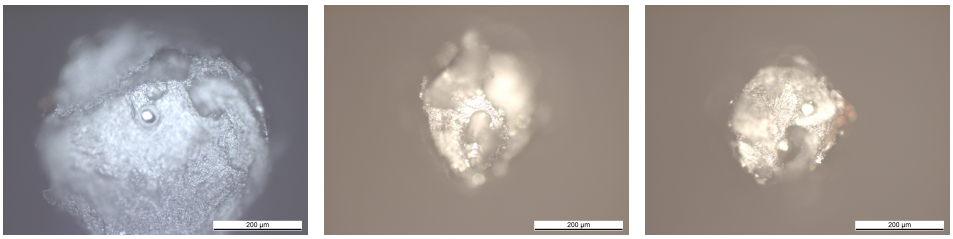

(d) Test 2 (e) Test 14 (f) Test 12.2

Figure 3.6: Six examples from six different strut samples for fracture surfaces with at least one inclusion present.

It is evident that the printing mechanisms are still prone to produce unwanted porosity in materials. These inclusions might be reduced with post-printing treatment like HIP.

3.2 Finite Element Analysis Results

For the analysis with FEA, the struts were simulated with different approaches as explained in chapter 2. First, the nominal geometry from CAD as it was sent to the printing company was calculated to see the notch effect of the original nominal design itself. As a second step, samples for which a μ-CT scan was available, were examined as well. Since the 200 μm struts are the weaker ones in terms of fatigue performance and out of time limitations, only those were used for the real strut FEAs.

3.2.1 Results for the Nominal Structure

Mesh Convergence Study and 200μm Notch Analysis

The first step for the nominal geometry was to run simulations for a mesh convergence analysis. At the same time, the induced nominal notch was analysed. The results are shown on the right with a picture of the Mises equivalent stress distribution over the whole sample in Figure 3.7 and in Figures 3.8 and 3.9 with charts of the simulation results. It was shown that for a mesh size below $0.0125mm$ the results stopped to change below a threshold of 0.115% for the Mises equivalent stress and 0.273% for the maximal principal stress values, which was concluded to be a satisfying convergence.

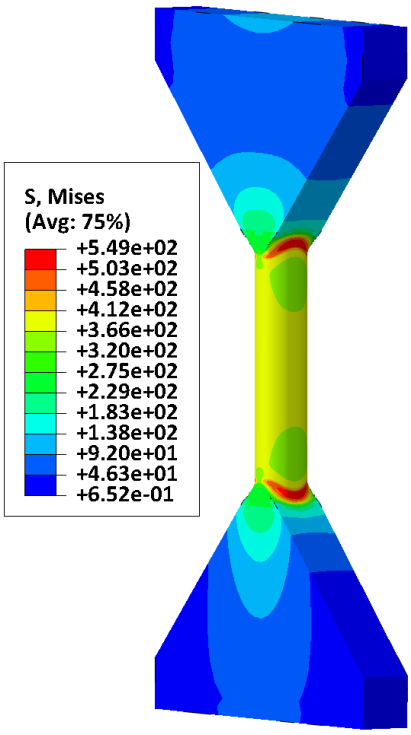

Figure 3.7: Stress distribution from FEA of nominal strut geomerty with 200μm diameter.

In comparison to the calculated theoretical K_t values, which lay in the interval of $[1.352, 2.049]$ (see section 2.2.2 on page 17), the simulated values are realistic placing themselves at 1.497 for the Mises and 1.572 for the maximal principal stresses calculated with the finest mesh.

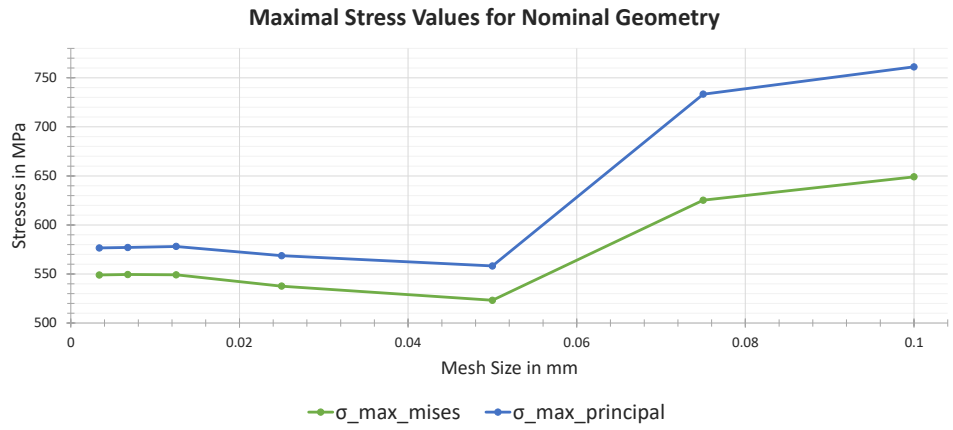

Figure 3.8: FEA mesh sensitivity and maximal notch stress analysis for nominal strut geometry of 200μm struts. For Mises equivalent and maximal principal stresses. Simulated with a loading equivalent to 366.7MPa nominal stress in the circular section.

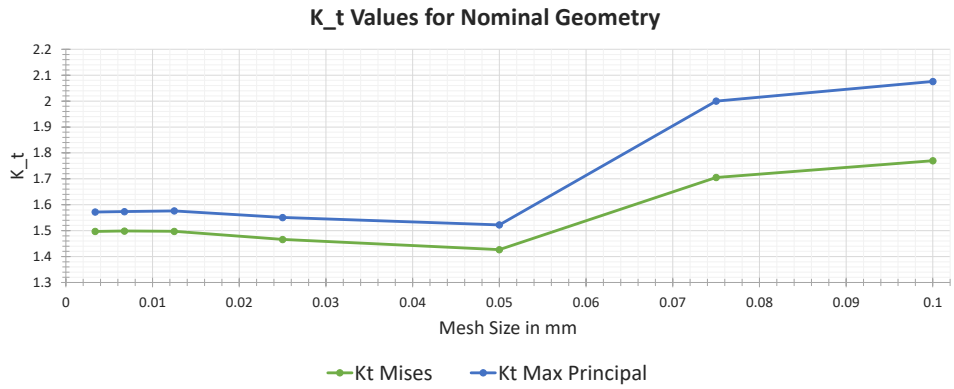

Figure 3.9: Mesh sensitivity on K_t factor for the nominal geometry notch of the 200μm struts. Calculated for Mises equivalent and maximal principal stresses.

Analysis for Size Effect of Nominal Geometry

As a next step, for the size effect analysis of the nominal geometry, additional simulations for 500 and 300μm struts were run. There as well the results were as expected according to the theory. The thicker the strut, the higher the K_t values. Figure 3.10 shows the three different diameters and their averaged K_t values with the indications of deviation between the upper and lower value of maximal principal and Mises equivalent stress concentra-

tion factor. All these values were as expected from the theoretical approach (see section 2.4.4 on page 26). In Figure 3.11 the simulated Mises equivalent stress distribution for the two geometries with larger diameters are shown.

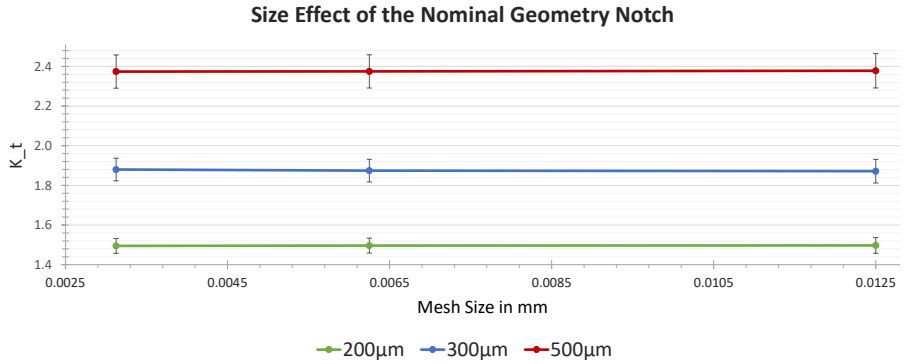

Figure 3.10: FEA results for size effect analysis of nominal strut geometry notch. Simulated for $200\mu m$, $300\mu m$ and $500\mu m$ diameter. Values for K_t averaged between Mises equivalent and maximal principal stress. Upper and lower bounds at each point indicated with bars.

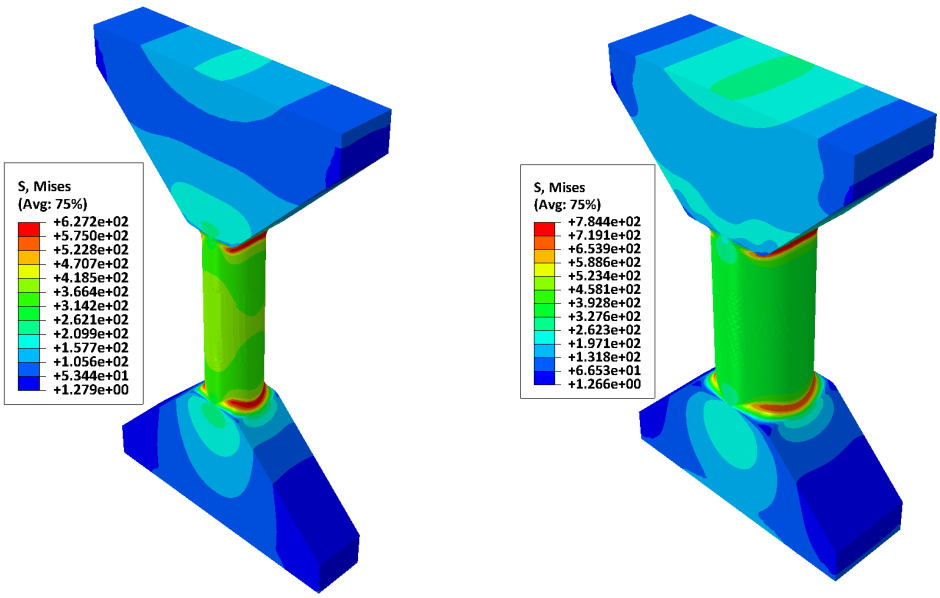

(a) $300\mu m$ (b) $500\mu m$

Figure 3.11: FEA results of the two additionally simulated thicknesses for the size effect analysis on the nominal structure.

3.2.2 Results for the Real Structure

The next step was to analyse the real printed and μ-CT scanned three dimensional geometry. This turned out to be not as straight forward as it was expected. The handling of scanned geometry, which can only be exported in STL file format, makes working with it rather difficult. Additionally, the generated and refined geometry is never as good to work with as a traditionally designed structure from CAD. The meshing of the struts poses a very difficult task to realize. This is due to the unconventional shapes and the minuscule mesh sizes required to adequately represent the geometry.

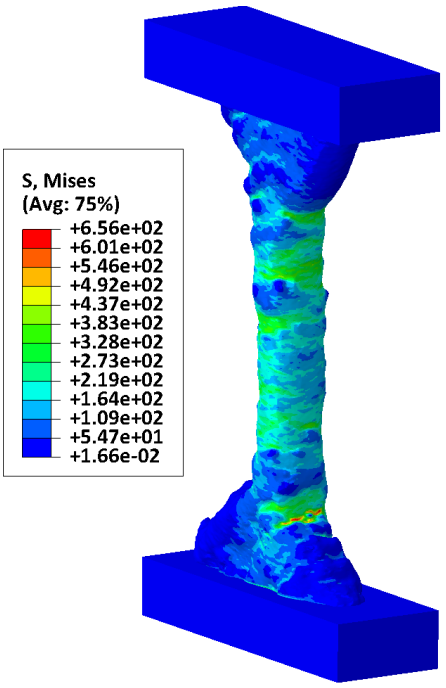

Figure 3.12: Stress distribution from FEA of μ-CT scan strut geometry.

Different software solutions to realize and mesh the geometry were iterated for the best solution, but sadly I could not find a definitive winner. Due to a matter of time, only two of the scanned struts could be simulated in a more or less satisfactory manner. The setup for the simulations of these struts is described with more detail in section 2.5.

The results which were achieved are displayed in the following two charts in Figures 3.14 and 3.15. Above in Figure 3.12 and on the right in Figure 3.13 the resulting stress distribution for one of the simulations are shown overall and in a close-up. In the latter, one the specific characteristics of AM samples is clearly visible, i.e. to have high stress concentrations in very small vicinities of the peak value. This is due to the printing induced notches and edges. Same as for the nominal struts a mesh sensitivity analysis was made for one strut (S_1_9_1). Subsequently, for another specimen the simulations for the determination of the K_t values were run.

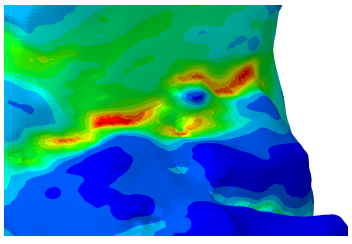

Figure 3.13: Close up of stress distribution around maximum location. The colour legend is equal to figure 3.12.

But as it is visible in Figure 3.15 for the second geometry, the mesh was not yet at a convergent level and further refinement would have been necessary. Due to the mentioned meshing problems and limitations in computational resources, these additional simulations could not be made.

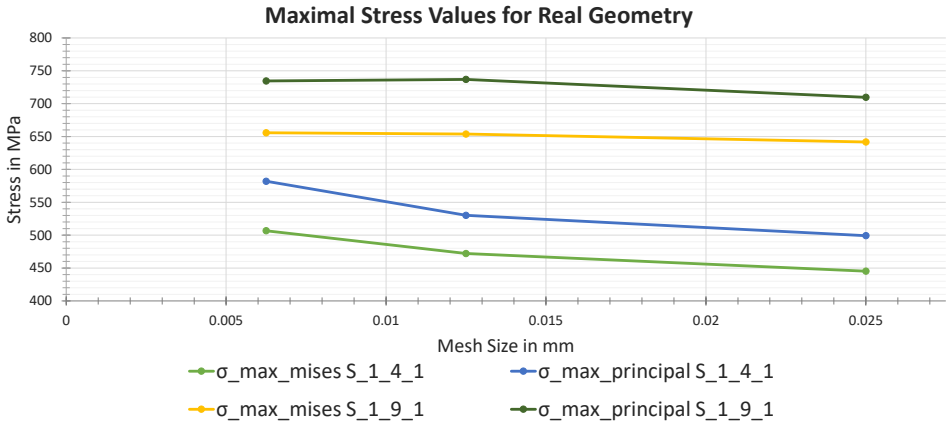

Figure 3.14: Maximal stress values for FEA simulated real μ-CT scanned geometries. Plotted are Mises equivalent and maximal principal stress for each specimen.

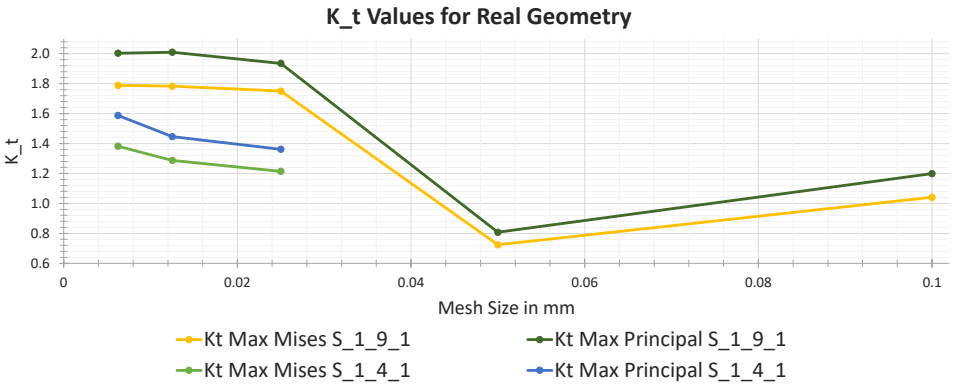

Figure 3.15: Mesh convergence analysis and K_t calculation with the reverence stress calculated for nominal diameter.

Even for a mesh size of $0.003125mm$, which equals to 1.6% of the nominal diameter, it could not be said with certainty that a satisfying convergence was reached. Possible approaches to get feasible simulations for this problem would include to locally refine the mesh around the critical notch, but there are two significant problems to this approach. On the one hand, that

it is never completely clear where exactly to refine the mesh beforehand. It occurred that the location of maximal stress changed its location after a new simulation with refined mesh was run. So running a coarse mesh simulation must not be sufficient to get the critical location correctly. On the other hand, for the local refinement, I do not know a working method. All the mesh refinement tools that are available in Abaqus or Siemens NX 12 are not made for refinement on these types of geometries. Also within the 3-Matics software, there is to my knowledge no such function to select only local geometries and refine them separately from the global mesh. Sub modelling approaches might be a solution, but for this approach getting the boundaries right, might be tricky.

Another question is whether it is reasonable to try and mesh the scanned geometry as close as possible. The transversion from the μ-CT pictures into the 3D geometry introduces geometry errors as well. This leads to the question, whether the refinement to smallest details down to the single μm is reasonable, while the scan itself is limited by finite resolution.

Chapter 4

Summary and Outlook

The objective of this thesis was to analyse the fatigue properties of SLM printed Ti-6Al-4V structures. In particular, the aim was to find a size effect between different thicknesses in AM single strut diameters and to further assess struts with FEA for the determination of a K_t factor for AM effects.

From the experiments, microscopic analysis and the FEA have led to the following findings:

- It is crucial to compare stress values calculated on real cross-sections between different strut sizes. Since oversizing is a big issue for geometries of this scale.
- Under consideration of real stress values, the larger specimens perform superior to the smaller ones.
- For the struts with the design of the nominal structure, a substantial notch is introduced at the connecting edges to the interesting middle part, which leads to local stress concentrations. This notch makes a proper analysis of the strut structure in between difficult.
- The approximative calculation of the influence of misalignment in the testing setup showed that there might be a significant discrepancy between the actually tested stress levels and the ones that should have been tested. This problem needs to be further investigated to quantify its effect on the testing results.
- The FEA of the real shape μ-CT scanned struts posed a bigger problem than expected. The small size of the specimens and their even finer detailed geometry brought large problems to the meshing of the geometry. Therefore only a limited analysis of the struts was realised.

For the future research projects, it could be interesting to search further for optimized processes to generate suitable meshes and get simulations results

with a feasible amount of computational power. Upon solving this task, the focus could be back on seeing whether the FEA's predicted maximal stress location coincides with the fracture location.

To further analyse the strut specimens, it could be interesting to additionally analyse samples, which were treated with post-printing treatments. Possibly printing oversized and using chemical etching to the aimed for diameters or to use HIP or even a combination of both. This could lead to interesting results since it reduces the waviness of the structure and its induced notches with the etching process and with the HIP the internal cavities might be reduced.

To analyse the actual effects of AM on the fatigue performance of cylindrical struts the influence of the nominal geometry and the testing setup would have to be minimized. Interesting approaches for the nominal geometry might be to implement a fillet between the support structure and the strut middle part as they are described in [14] on pages 140-142. To reduce the notch effect to a nonsignificant level. For the testing setup problem, a self-aligning setup could be a possible solution (realized with the usage of two spherical joints maybe).

Another interesting topic could be to find out what influences the limits of an AM SLM printer in terms of geometric dimensions. In correlation to the size of the lasers' smelting pool, the printing powder grain size and layer thickness. As for other more conventional manufacturing methods these machine and tool-specific limitations have to be taken into account. It might show to be reasonable to invest more time into the consideration of the printing limitations and to optimize accordingly while designing an AM structure. This way the overall geometry defects and mismatches could possibly be minimized.

Appendix A

Calculation of Induced Stresses from Misalignment

A.1 Simplified Hand Calculation

The assumptions for the hand calculation of the induced stresses due to a misalignment are the following:

- The strut is considered as a circular linear elastic beam.
- The diameter is constant as it is in the nominal geometry.
- The misalignment, one side of the clamping mechanism to the other, is fixed at $0.03mm$, roughly the size of a thin hair. This leads to an angle between the dynamic axis and the center axis of the strut.
- Only the effect of the induced part of the force normal to the centerline is considered in the calculations
- It is assumed that the beam is clamped on one side and free on the other.
- A uniaxial stress state is assumed (only in x-direction).

All the assumed parameters for the calculation are listed in the following table:

Table A.1: Parameters for the stress calculation induced through misalignment for the $200\mu m$ and $500\mu m$ struts.

Young's Modulus	E	$100GPa$
Radius	R	$0.1mm$ and $0.25mm$
Length	l	$1mm$
Unclamped Distance	d	$6mm$
Misalignment	Δw	$0.05mm$
Experimental Force	F_{exp}	-26N and -96N
Area Moment of Inertia	$I_y = I_z$	$\frac{\pi R^4}{4}$

With basic geometry, the angles of a right triangle are calculated from its catheti with the tangent function. The length over which the misalignment takes place is $6mm$ as is was set to for each experiment. Therefore the angle of misalignment γ is:

$$\gamma = \arctan \frac{\Delta w}{d} \approx 0.477^\circ$$

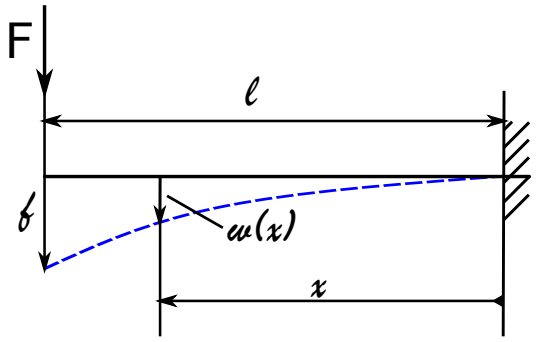

Figure A.1: Simplified assumption for misalignment stress calculation.

Therefore the testing force can be split up into a parallel and a normal component relative to the specimens centerline. Only the normal component is being analysed here:

$$F = \sin\gamma * F_{exp} \approx 0.008 * F_{exp}$$

From basic mechanics lectures, the formulas for a linear elastic beam, as it is shown in Figure A.1, are known. With the previously calculated forces the induced bending torque at the clamped side can be calculated:

$$M_b(x = 0) = -l * F = -l * \sin\gamma * F_{exp}$$

With the value for the induced bending torque, one can calculate the induced stresses at the fixed position. They distribute linearly over the cross-section in $y - z - plane$ with zero stress in the middle and the maximum value on top and the minimum on the bottom:

$$\sigma_x(y) = -\frac{M_z}{I_z}y = \frac{l * \sin\gamma * F_{exp}}{I_z}y \quad \Rightarrow \quad \sigma_{x,max} = \frac{4 * R * l * \sin\gamma * F_{exp}}{R^4 * \pi}$$

$$\Rightarrow$$

$$\sigma_{x,\ max,\ 200\mu m} = 275.8MPa$$

$$\sigma_{x,\ max,\ 500\mu m} = 65.17MPa$$

Considering the oversizing according to [5] for the $200\mu m$ struts this reduces to:

$$\sigma_{x,\ max,\ 200\mu m} = 77.0MPa$$

This state has to be superposed with the stress from to the parallel force and then one gets an estimate for the stress-changes they are listed in Table A.2.

Table A.2: Maximal nominal stress values if induced bending is considered. For the $200\mu m$ struts additionally, the oversized nominal diameter was considered. Because of the extremely high values for the unchanged area.

	no bending in MPa	with bending in MPa	additional stress in %
$500\mu m$	488.89	554.08	13.33
$200\mu m$	827.61	1103.44	33.33
oversized $200\mu m$	353.54	430.56	21.78

Following up on the next page, the FEA for the misalignment is described.

A.2 FE Simulation

A single FE Simulation was made, where the force was split up in parallel and normal parts, according to the misalignment angle from the hand calculation before in A.1. The results as shown in Figure A.2 are higher than the approximative hand calculation. But the nominal geometry is additionally to the bending influenced by its notch as discussed in section 3.2.1. This affects the situation further. Nevertheless, the distribution shows a clear asymmetrical stress allocation with significant stress concentrations.

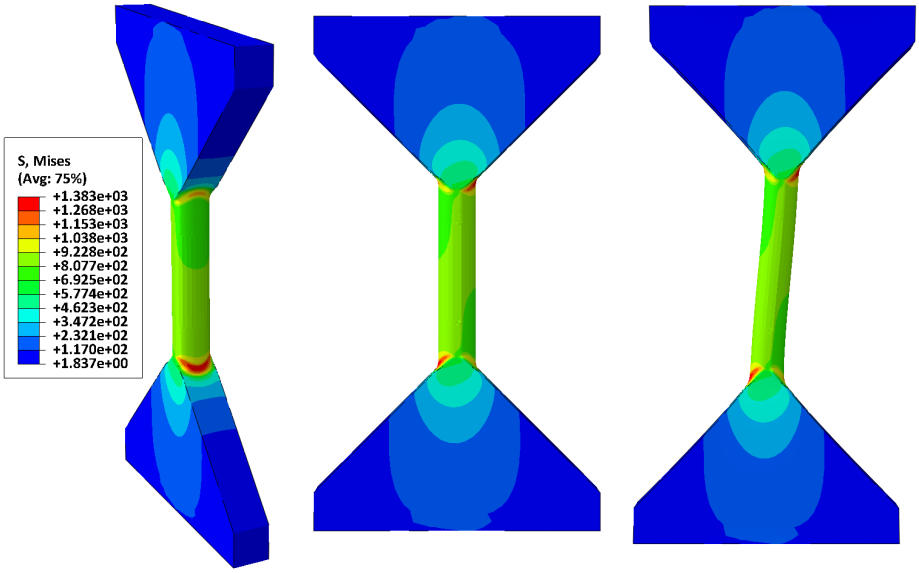

Figure A.2: FE simulation of misalignment in testing setup.

Bibliography

[1] Adam, Guido A.O. and Zimmer, Detmar. Design for additive manufacturing — element transitions and aggregated structures. *CIRP Journal of Manufacturing Science and Technology*, 7(1):20 – 28, 2014.

[2] Berger, Christina. *Bruchmechanischer Festigkeitsnachweis für Maschinenbauteile : FKM-Richtlinie*. VDMA Verlag GmbH, Frankfurt am Main, 4. ausgabe edition, 2018.

[3] Ehsan, Hosseini. *Metal Additive Manufacturing - Lecture 1 - Introduction to Additive Manufacturing.* 2019.

[4] Frost, N. E. et al. *Metal Fatigue.* Clarendon Press, 1974.

[5] Ghedalia, Daniele. Characterization and modeling of orientation and size dependent tensile behavior of AM Ti6Al4V, 8 2019.

[6] Greenfeld, Daniel. Fatigue behavior investigation of additively manufactured Ti-6Al-4V lattices, 7 2019.

[7] Huffman, Peter. *A quantitatively accurate theory of stable crack growth in single phase ductile metal alloys under the influence of cyclic loading*. PhD thesis, 2014.

[8] Li, P. and Warner, D. H. and Fatemi, A. and Phan, N. Critical assessment of the fatigue performance of additively manufactured ti–6al–4v and perspective for future research. *International Journal of Fatigue*, 85:130 – 143, 2016.

[9] Lohmuller, Paul and Favre, Julien and Piotrowski, Boris and Kenzari, Samuel and Laheurte, Pascal. Stress Concentration and Mechanical Strength of Cubic Lattice Architectures. *MATERIALS*, 11(7), JUL 2018.

[10] Najmon, Joel C. and Raeisi, Sajjad and Tovar, Andres. 2 - review of additive manufacturing technologies and applications in the aerospace industry. In Francis Froes and Rodney Boyer, editors, *Additive Manufacturing for the Aerospace Industry*, pages 7 – 31. Elsevier, 2019.

[11] Paramore, James D. and Fang, Zhigang Z. and Dunstan, Matthew and Sun, Pei and Butler, Brady G. Hydrogen-enabled microstructure and fatigue strength engineering of titanium alloys. *Scientific Reports*, 7:41444 EP –, Feb 2017. Article.

[12] Paris, P. and Erdogan, F. A Critical Analysis of Crack Propagation Laws. *Journal of Basic Engineering*, 85(4):528–533, 12 1963.

[13] Pelleg, Joshua. *Mechanical properties of materials*, volume vol. 190 of *Solid mechanics and its applications*. Springer, Dordrecht, 2013.

[14] Peterson, Rudolph E. *Peterson's stress concentration factors.* 2008.

[15] Robmann, Serjosha. Deformation Analysis and Finite Element Modelling for Ti-6Al-4V Additive Manufactured Lattices, 8 2019.

[16] Ruge, Jürgen and Wohlfahrt, Helmut. *Technologie der Werkstoffe : Herstellung, Verarbeitung, Einsatz ; mit ... 62 Tabellen*. 2013.

[17] Schijve, Jaap. *Fatigue of Structures and Materials.* 2004.

[18] Wunderlich, Walter and Pilkey, Walter D. *Mechanics of structures : variational and computational methods*. CRC, Boca Raton, 2nd ed. edition, 2003.

List of Figures

List of Tables

Eidgenössische Technische Hochschule Zürich
Swiss Federal Institute of Technology Zurich

Declaration of originality

The signed declaration of originality is a component of every semester paper, Bachelor's thesis, Master's thesis and any other degree paper undertaken during the course of studies, including the respective electronic versions.

Lecturers may also require a declaration of originality for other written papers compiled for their courses.

I hereby confirm that I am the sole author of the written work here enclosed and that I have compiled it in my own words. Parts excepted are corrections of form and content by the supervisor.

Title of work (in block letters):

Fatigue Analysis of Selective Laser Melted Ti6Al4V Structures

Authored by (in block letters):

For papers written by groups the names of all authors are required.

Name(s):	**First name(s):**
Thalmann	Max

With my signature I confirm that

- I have committed none of the forms of plagiarism described in the 'Citation etiquette' information sheet.
- I have documented all methods, data and processes truthfully.
- I have not manipulated any data.
- I have mentioned all persons who were significant facilitators of the work.

I am aware that the work may be screened electronically for plagiarism.

Place, date	**Signature(s)**
Zürich, 14. February. 2020	

For papers written by groups the names of all authors are required. Their signatures collectively guarantee the entire content of the written paper.